Journal of Sound and Vibration 476 (2020) 115290

Contents lists available at ScienceDirect

Journal of Sound and Vibration

journal homepage: www.elsevier.com/locate/jsvi

Scaling laws of electromagnetic and piezoelectric seismic vibration energy harvesters built from discrete components

P. Gardonio*, L. Dal Bo

Università degli Studi di Udine, DPIA, Via delle Scienze 208, 33100, Udine, Italy

ARTICLE INFO

Article history:
Received 16 July 2019
Received in revised form 24 February 2020
Accepted 27 February 2020
Available online 7 March 2020
Handling Editor: Sang Woo Han

Keywords:
Seismic vibration energy harvesting
Vibration energy harvesting scaling laws
Electromagnetic seismic vibration harvester
Piezoelectric seismic vibration harvester

ABSTRACT

This paper presents a theoretical study on the scaling laws of electromagnetic and piezoelectric seismic vibration energy harvesters, which are assembled from discrete components. The scaling laws are therefore derived for the so called meso-scale range, which is typical of devices built from distinct elements. Isotropic scaling is considered for both harvesters such that the shape of the components and of the whole transducers do not change with scaling. The scaling analyses are restricted to the case of linearly elastic seismic transducers subject to tonal ambient vibrations at their fundamental natural frequency, where the energy harvesting is particularly effective. Both resistive-reactive and resistive optimal electric harvesting loads are considered. The study is based on equivalent formulations for the response and power harvesting of the two transducers, which employ the so called electromagnetic and piezoelectric power transduction factors, Π_{cm}^2 and Π_{pe}^2. The scaling laws of the transduction coefficients and electrical and mechanical parameters for the two transducers are first provided. A comprehensive comparative scaling analysis is then presented for the harvested power, for the power harvesting efficiency and for the stroke of the two harvesters. Particular attention is dedicated to the scaling laws for the dissipative effects in the two harvesters, that is the Couette air losses and eddy currents losses that develop in the electromagnetic harvester and the material, air and dielectric losses that arise in the piezoelectric harvester. The scaling laws emerged from the study, are thoroughly examined and interpreted with respect to equivalent mechanical effects produced by the harvesting loads.

1. Introduction

During the past two decades a very large number of prototype seismic vibration energy harvesters have been presented and investigated in scientific publications (e.g. see review articles in Refs. [1–9] and books in Ref. [10–14]). In general, seismic vibration energy harvesters use three types of transducers: electromagnetic, piezoelectric and electrostatic [1–15]. Magnetostrictive transducers are also employed in some cases, but comparatively fewer practical applications have been investigated up to present [5,9,15]. Several configurations, geometries and dimensions have been proposed over the years [2–9,11,12,14,16] (for example see Tables A1, A2 in Ref. [16]). In general, the overall size of the proposed devices covers a rather wide range that goes from characteristic dimensions of the order of few millimetres to a few decimetres. The smaller scale

* Corresponding author.
E-mail address: paolo.gardonio@uniud.it (P. Gardonio).

https://doi.org/10.1016/j.jsv.2020.115290

seismic harvesters (often called micro-scale harvesters [17]) are normally fabricated as monolithic devices with *Micro Systems Technology* (MST), which enables the shaping of micro-scale elements/layers forming the harvester (e.g. finger comb electrostatic transducers, folded springs, piezoelectric films, etc., having micrometric dimensions) [10]. Typically, they are fabricated on silicon substrates with deposition, patterning, etching processes followed by die preparation. Alternatively, the larger scale seismic harvesters (often called meso-scale harvesters [17]) are assembled from discrete elements manufactured with classical processes starting from raw materials (metal and plastic components, *Printed Circuit Boards* (PCB) and electric components, electric wirings, etc.) [10,13]. Because of the large surface area to volume ratio, small scale (i.e. micro-scale) MST seismic harvesters normally employ electrostatic transducers [10,13], although in some cases piezoelectric thin films have also been successfully used [18,19]. Their dynamic response is largely affected by surface tension and viscous fluid effects. Alternatively, larger scale (i.e. meso-scale) seismic harvesters are normally fabricated from discrete components and typically incorporate electromagnetic [11,13,14] and piezoelectric-patch [10–13] transducers. The dynamic response of these systems is often affected by hysteresis phenomena produced, for example, by eddy currents in the electromagnetic transducers [20–22] or dielectric losses in the piezoelectric transducers [23–26]. Although the electromechanical responses of the smaller scale MST seismic harvesters and larger scale assembled seismic harvesters present similarities and, thus, could be studied considering similar electromechanical models (e.g. see Refs. [1,3,6–15,27–32]), the phenomena listed above draw a separation line for the two types of devices, so that, as discussed in Ref. [17], specific physical models become necessary to accurately describe their responses and energy harvesting properties. Furthermore, the comprehensive scaling analysis carried out by Moss et al. [16] on a vast ensemble of prototype harvesters, clearly indicated that the responses and energy harvesting properties of each type of harvester (i.e. electrostatic, electromagnetic, piezoelectric, magnetostrictive) may vary substantially even for equivalent scale devices, depending on the specific design of the transducer.

Therefore, this paper presents a specific scaling study of typical larger scale (i.e. meso-scale) electromagnetic or piezoelectric seismic vibration harvesters assembled from discrete components. More specifically, the electromagnetic harvester encompasses a classical coil-magnet seismic transducer, which is formed by an inner cylindrical magnet and an outer ferromagnetic ring and coil assembly connected via soft axial springs. Instead, the piezoelectric seismic transducer comprises a cantilever composite beam, with a steel substrate and top and bottom piezoelectric layers, and a tip block mass. The study is based on detailed lumped parameter models and mathematical formulations of the constitutive electromechanical equations for the two seismic transducers, which were derived and validated experimentally in Ref. [33]. More specifically, the two models consider a mass-spring-damper-mass mechanical network and a resistive-inductive or a capacitive electrical mesh, which are connected via ideal electromagnetic or piezoelectric transducers. As shown in Ref. [33], the lumped parameters are derived from a detailed analysis of the electro-mechanical responses of two prototype transducers. For instance, the model for the electromagnetic transducer accurately takes into account the Couette air losses that develop in the air gap between the inner magnet and outer coil-ferromagnetic ring assembly and the eddy currents losses that develop in the coil and in the outer ferromagnetic ring [20–22]. Alternatively, the model for the piezoelectric transducer encompasses a modal mass, a modal stiffness and modal transduction factor for the fundamental flexural mode of the composite cantilever beam and tip mass assembly. Also, it incorporates the material, air and dielectric losses that arise in the beam and piezoelectric layers respectively [12]. All these are rather important effects, which are normally modelled considering the static elastic effects or simple viscoelastic and resistive dissipative effects (e.g. see Refs. [1,3,6–8,10–15,27–32]), although they are characterised by quite specific features that play an important role in the electromechanical response of the transducers and thus in the energy harvesting, particularly when the fundamental natural frequency of the transducers is set to match the frequency of tonal base vibrations. In this respect, the models consider linear elastic effects only. In fact, energy harvesting from tonal vibrations at the fundamental natural frequency of the transducer does not benefit from non-linear elastic effects, which would unnecessarily broaden the frequency band of the transducer resonant response at the expenses of unstable (jump phenomenon), and in some cases lower, peak responses. Indeed, non-linear elastic effects are normally employed to enhance vibration energy harvesting from broad-band ambient vibrations [34]. Also, the models consider only the resonant response of the transducer fundamental natural mode, which, as shown in Ref. [33], provides the maximum power harvesting effect. Again, a multi-resonant transducer would be beneficial for broadband vibration energy harvesting only [34].

The scaling laws of the electromagnetic and piezoelectric seismic harvesters are obtained under the assumption of steady state harmonic oscillations at the transducers fundamental natural frequencies, that is in condition of maximum energy harvesting for harmonic ambient vibration. Two configurations of the harvesting circuits are considered, which are characterised either by a complex or a purely real optimal impedance load set to maximise the harvested power. An isotropic scaling is assumed for either transducers such that their shapes do not change as the dimension of the devices are scaled. The notation described in Refs. [35–37] is used such that the scaling laws are obtained with reference to a single variable L, which represents the linear scale of the whole device. Numerical simulations are performed starting from the geometries and physical data of the prototype electromagnetic and piezoelectric seismic transducers modelled and studied in Ref. [33]. These transducers were designed and built in such a way as they have similar weights and similar volumes, i.e. $\approx$ 330 g and $\approx$ 60 cm^3, and about the same fundamental natural frequencies, i.e. $\approx$20 Hz. In this paper the scale L = 1 is thus referred to the characteristic dimension of these two prototypes, which can be assumed equal to 4 cm . Also, considering the dimensions of typical transducers for energy harvesting applications reported in literature [5,16,38–43], the scaling range considered in this study has been fixed between 4×10^{-1} and 4×10^{1} cm. As proposed by Beeby et al. [43], the power scaling analysis is performed by normalizing the harvested power to the total volume of the device and to the amplitude of the input

acceleration squared. More specifically, this normalised power density function is assessed at the fundamental natural frequency of the two seismic transducers to provide a practical figure of merit for the maximum energy that can be harvested by the two types of harvesters.

The paper is structured in seven sections. Section 2 briefly describes the two seismic harvesters and recalls the lumped parameter models and constitutive equations for the electromechanical responses of the two seismic transducers. Also, it introduces the so called "power transduction factors" for the two transducers, which provide a figure for the ratio between the electrical-to-mechanical and mechanical-to- electrical power exchange and the electrical and mechanical power input in the two transducers at hand. The two coefficients are then effectively used to derive a unified formulation for the power harvested and harvesting efficiency for the two harvesters. Sections 3 and 4 present equivalent scaling studies for the two seismic harvesters. Hence, both sections start by introducing the energy formulations used to derive the power expressions for the scaling study. They then present an overview of the scaling laws for the mechanical, electrical and transduction physical effects that characterise the two seismic transducers. Finally, they provide comprehensive scaling studies for the power harvesting and for power harvesting efficiency when the two harvesters implement optimal electric loads set to maximise the harvested power. A comparative study is then proposed in Section 5 to contrast the power harvesting and the power harvesting efficiency of the two devices, with reference to scale. Finally, section 6 produces a scaling study of the strokes that characterise the two transducers, which also play a key role on the effective power harvesting with the two devices. The geometry and physical characteristics of the reference electromagnetic and piezoelectric transducers with characteristic scale $L = 1$ are summarised in Appendix A. Also, Appendix B derives the frequency of maximum power harvesting with the two seismic transducers.

2. Seismic harvesters: lumped parameter models, constitutive equations and power transduction factors

This section describes the electromagnetic and piezoelectric harvesters and the lumped parameter models used to derive their electromechanical responses and power functions. Also, it defines the constitutive equations that characterise the two systems and provides spectral analyses to illustrate the principal properties of the harmonic response of the two transducers. Finally, it introduces the so called power transduction factors, which provide the inherent power transfer properties for electromagnetic and piezoelectric transductions.

2.1. Seismic harvesters and lumped parameter models

The top sketches in Fig. 1 show the electromagnetic and piezoelectric seismic transducers considered in this study, which represent typical designs employed for energy harvesting applications. As indicated in sketch (a), the electromagnetic seismic harvester is composed by a core cylindrical magnet and an outer ferromagnetic cylindrical ring (armature) with a double coil on the inner side [44]. The two components are connected to each other via two spiral springs that produce a soft axial

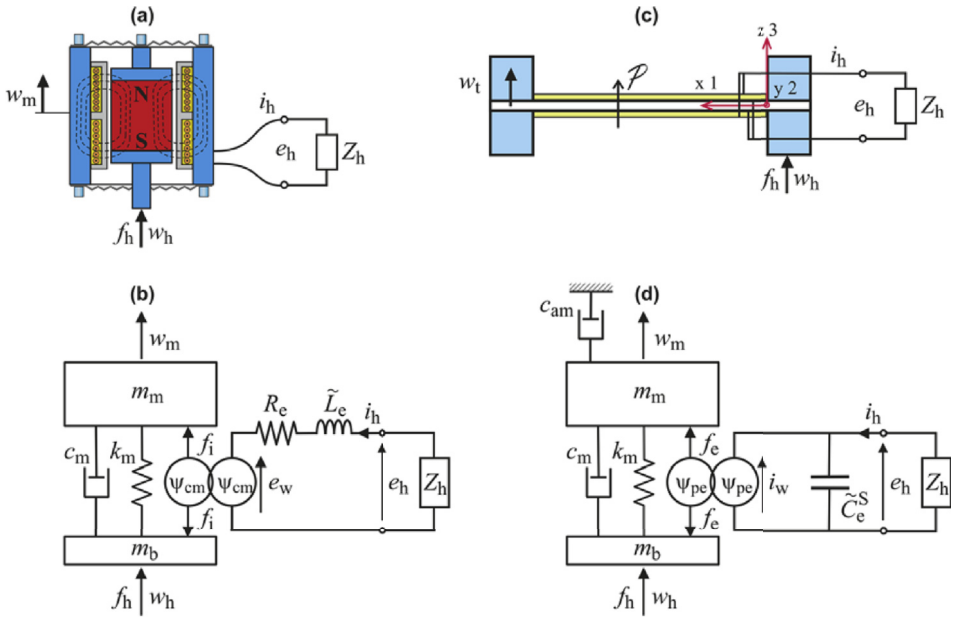

Fig. 1. Sketches (a,c) and lumped parameter schematics (b,d), of the electromagnetic (left hand side) and piezoelectric (right hand side) seismic transducers considered in this study.

stiffness and a very high transverse stiffness. The relative axial motion between the magnet and the coil produces a back electromotive force, i.e. a voltage, at the terminals of the coil. In some applications, the magnet is the moving component whereas the coil is fixed to the base. Often, for this configuration, the magnet is connected to an external ferromagnetic ring via a top ferromagnetic disc and the coil is housed in the gap between the inner cylinder and the outer ring (e.g. see Refs. [14,45,46]). Nevertheless, as can be noticed from Refs. [33,47,48], despite these differences, the two configurations operate in a very similar manner and are normally studied with equal lumped parameter models as that shown in Fig. 1b.

As shown in the sketch (c), the piezoelectric seismic harvester is made by a composite beam with block masses fixed at the base and free ends. The beam is formed by a thin steel substrate, of thickness h_s, with piezoelectric layers, of thickness h_{pe}, bonded on the top and bottom faces, which are electrically connected in parallel. In this case, the relative motion between the base mass and the tip mass generates a bending strain of the cantilever composite beam, which, in turn, produces a separation of electric charges in the electrodes of the piezoelectric layers. Both transducers are equipped with an electric harvesting load characterised by either a complex or a purely real impedance Z_h.

As shown in Fig. 1(b) and (d), the two transducers are modelled using lumped parameter electromechanical models, which encompass a mechanical assembly and an electric mesh coupled via ideal transduction elements. Considering first the lumped parameter model for the electromagnetic harvester shown in Fig. 1b, the mechanical assembly is formed by a base mass m_b and a seismic mass m_m connected by a spring k_m and damper c_m in parallel. The electric mesh is formed by a resistor R_e and lossy inductor $\tilde{L}_e$ in series. The two networks are connected to each other via a *current-controlled ideal reactive force generator* and a relative *velocity-controlled ideal voltage generator*, which are characterised by the transduction coefficient ψ_{cm} [33]. The base mass accounts for the mass of the core cylindrical magnet component and half mass of the two spiral springs. Also, the moving mass includes the mass of the outer ferromagnetic ring, the mass of the coil winding and half mass of the two spiral springs. Thus, the two masses are given by:

$$m_b = \rho_m V_m + \rho_s V_s, \tag{1}$$

$$m_m = \rho_r V_r + \rho_c V_c + \rho_s V_s, \tag{2}$$

where ρ_m, ρ_r, ρ_c ρ_s and V_m, V_r, V_c, V_s are de densities and volumes of the magnet, outer ring, coil and springs components. The spring takes into account the aggregate bending stiffness of the two spiral springs and, according to Ref. [37], is given by:

$$k_m = 2\frac{3Y_k A_k}{h_k}, \tag{3}$$

where Y_k is the material Young's modulus of elasticity, A_k is cross section area and h_k is the length of the spirals. The damper takes into account two effects: first the Couette air flow damping that develops in the thin gap between the inner magnetic cylinder and the coil winding built in the outer ferromagnetic ring [37,49] and, second, the eddy currents damping due to the eddy currents that develop in the ferromagnetic ring [50–52]. For the scale range considered in this study, the sky-hook air damping that develops on the exterior surface of the moving ferromagnetic ring and the material energy loss that arises in the flexible spiral springs are comparatively much smaller than the Couette airflow and eddy currents damping effects, therefore they are neglected in the lumped model of Fig. 1b. Thus the damping coefficient c_m can be written as the sum of the damping coefficients for the Couette airflow and eddy currents damping:

$$c_m = c_a + c_{ec}. \tag{4}$$

Considering first the Couette air flow damping, as shown in Refs. [1,49], a Newtonian viscous fluid contained between two surfaces in relative motion is subjected to a constant stress and undergoes a *Couette laminar flow* that varies linearly across the two surfaces such that the Couette air flow damping coefficient is given by

$$c_a = \mu_c \frac{A_c}{d_c}, \tag{5}$$

where μ_c is the fluid viscosity, A_c is the lateral surface of the magnetic cylinder and d_c is the radial gap between the inner magnetic cylinder and the outer coil and ferromagnetic ring. Moving to the eddy currents damping, as discussed in Refs. [40,53], provided the inner cylindrical magnet maintains the same aspect ratio, the magnitude B_r and the field gradient ∇B_r of the magnetic field density remains constant and decreases as the dimension of the magnet is raised respectively. However, the presence of a diffusion phenomenon, due to the interaction of the eddy currents with the magnetic field generated by the magnet, produces an exponential decrement of the current density in radial direction of the outer ferromagnetic ring. In this case, the eddy currents damping coefficient c_{ec} [50–52] can be derived with the following integral expression:

$$c_{ec} = 2\pi\sigma_e \int_{-\frac{H_r}{2}}^{\frac{H_r}{2}} \int_{R_i}^{R_i+\delta} r B_r^2(r,z)\, \mathrm{d}r\mathrm{d}z, \tag{6}$$

where H_r and R_i are the height and inner radius of the ferromagnetic ring, δ is the so called skin depth [54] and r, z are the radial and axial coordinates. The resistor encompasses the resistive effect of the coil winding, thus:

$$R_e = \frac{\rho_e l_r}{A_r}, \tag{7}$$

where ρ_e is the resistivity and A_r, l_r are the cross section and the length of the wire. References [20–22] showed that the coil winding is also affected by eddy currents such that a lossy inductor model should be employed, which is characterised by a complex inductance given by

$$\tilde{L}_e(\omega) = L_e^{'}(1 - \mathrm{j}\eta_L), \tag{8}$$

where

$$L_e^{'} = L_e \sin(n\pi/2)\omega^{n-1}, \tag{9}$$

$$\eta_L = \frac{\cos(n\pi/2)}{\sin(n\pi/2)}. \tag{10}$$

The inductance L_e of a N-turns coil, with radius R_c and wire length l_c, can be derived recalling that $L_e = N\Phi/i$, where the self-flux generated inside the coil is $\Phi = NB_x\pi R_c^2$ and the magnetic flux density generated by the current i is given by $B_x = \mu_e Ni/l_c$, where μ_e is the permeability of the magnet, such that [35]:

$$L_e = \mu_e \frac{N^2 \pi R_c^2}{l_c}. \tag{11}$$

The factor n in Eqs. (9), (10) is normally derived from system identification of real coil elements and is comprised between 0 and 1. In general, for $n = 0$ the inductor acts as a resistor whereas for $n = 1$ it performs as a lossless inductor. Finally, the electromagnetic transduction is characterised by a constant coefficient, which is given by the product between the radial magnetic flux density B and the length of the coil winding l_c [55–58]:

$$\psi_{cm} = Bl_c. \tag{12}$$

Moving to the piezoelectric transducer, as discussed in Ref. [33], the flexural response of the composite cantilever beam and tip mass is characterised by the superposition of the second order responses of multiple flexural natural modes. Nevertheless, for tonal ambient vibrations, to maximise the energy harvesting, the transducer is normally set in such a way as the resonance frequency of the fundamental flexural mode coincides with the frequency of the tonal ambient vibration. Therefore, the transducer can be suitably modelled considering only the physical parameters that characterise the second order response of the fundamental flexural natural mode of the composite cantilever beam and tip mass. Accordingly, as shown in Fig. 1d, the lumped parameter model for the piezoelectric transducer encompasses a mechanical assembly, which is formed by a base mass m_b and a seismic mass m_m connected to each other by a spring k_m and damper c_m in parallel, and an electric mesh, which is made by a lossy capacitor $\tilde{C}_e^S$. The seismic mass is also connected to a sky-hook damper c_{am}. In this case the two networks are connected via a *current-controlled ideal reactive force generator* and a relative *velocity-controlled ideal current generator*, which are characterised by the transduction coefficients ψ_{pe}. As discussed in details in Ref. [33], the base mass is given by:

$$m_b = \rho_b V_b, \tag{13}$$

where ρ_b and V_b are de densities and volumes of the base block. The moving mass is given by the equivalent mass of the first natural bending mode of the composite beam and tip block assembly, which was derived in Ref. [33] as follows:

$$m_m = \frac{1}{\phi_1^2(\bar{x})} \left\{ \int_0^L m\phi_1(x)\phi_1(x)dx + M_t\phi_1^2(L) \right\}. \tag{14}$$

Here $m = b(\rho_s h_s + 2\rho_{pe} h_{pe})$ is the mass per unit length of the composite beam, which depends on the substrate and piezoelectric layers densities ρ_s, ρ_{pe}, the thicknesses h_s, h_{pe} and the width b. Also, M_t is the tip mass, which is given by $M_t = \rho_t V_t$, where ρ_t and V_t are de densities and volumes of the tip block. Moreover, $\phi_1(x)$ is the first bending mode of the clamped composite beam and tip mass whose expression can be found in Ref. [33]. Finally, L is the length of the beam and $\bar{x} = 0.9L$. The modal stiffness of the first bending mode of the composite beam and tip mass assembly is derived recalling that the natural

frequency of the mode is given by the following expression $\omega_n = \sqrt{k_m/m_m}$. The natural frequency was derived in Ref. [33] as follows:

$$\omega_n = \frac{\lambda_1^2}{L^2}\sqrt{\frac{B}{m}}, \tag{15}$$

where $B = Y_s I_s + Y_{pe}^E I_{pe}$ is the bending stiffness of the composite beam, which depends on the substrate and piezoelectric layers moduli of elasticity Y_s and Y_{pe}^E and cross area second moment of inertia: $I_s = \frac{bh_s^3}{12}$ and $I_{pe} = \frac{2}{3}b\left[\left(\frac{h_s}{2}+h_{pe}\right)^3 - \frac{h_s^3}{8}\right]$. The coefficient λ_1^2 was calculated from the implicit characteristic equation derived assuming free flexural vibrations of the cantilever beam and tip mass. Therefore the modal stiffness k_m for the first flexural mode of the clamped composite beam and tip mass results:

$$k_m = \omega_n^2 m_m. \tag{16}$$

Finally, the damper c_m includes the internal strain-rate damping due to the hysteresis effect caused by the relaxation and creep phenomena of the steel and piezoelectric materials whereas the damper c_{am} encompasses the external sky-hook viscous air damping exerted on the beam. The strain-rate damping is normally modelled in terms of a complex stiffness [59,60], which for the model at hand results $k_m(1 + j\eta_m)$, where η_m is the loss factor. However, for harmonic vibration, a Kelvin–Voigt model with a spring and damper in parallel can be employed [12], where the damper is characterised by a damping factor

$$c_m = \frac{\eta_m\, k_m}{\omega_n}. \tag{17}$$

For the scale range considered in this study, the damping effect generated by the air loading on the beam can be derived by calculating the integral over the beam surface of the acoustic pressure exerted on the first flexural mode of the composite beam and tip mass by the vibration of the same mode, where the radiated sound pressure is given by the Rayleigh integral [61], so that:

$$c_{am} = \mathrm{Re}\left\{\frac{j\omega\rho_0}{2\pi}\int_0^L\int_0^L b^2\phi_1^2(x)\frac{e^{-jk|x-x'|}}{|x-x'|}\mathrm{d}x\mathrm{d}x'\right\}. \tag{18}$$

Here ρ_0 is the density of air, $k = \frac{\omega}{c_0}$ is the acoustic wave number and c_0 is the speed of sound in air. The capacitor is modelled in terms of a complex capacitance $\tilde{C}_e^S$ which takes into account both the capacitive and the dielectric losses effects that arise in the piezoelectric layers [22–25]. More specifically the lossy capacitance is given by

$$\tilde{C}_e^S = C_e^S(1 - j\eta_c), \tag{19}$$

where the capacitance of the piezoelectric layers under constant strain and the dielectric loss factor are given by

$$C_e^S = C_e^T\left(1 - k_{31}^2\right) \tag{20}$$

$$\eta_C(\omega) = \frac{\sigma_{pe}}{\varepsilon_{33}^S\omega} \tag{21}$$

Here k_{31}^2 is the 31 electromechanical coupling factor of the piezoelectric material [55], σ_{pe} is the electrical conductivity of the piezoelectric material and $\varepsilon_{33}^S = \varepsilon_{33}^T(1 - k_{31}^2)$ and ε_{33}^T are the permittivity of the piezoelectric material in transverse direction under constant strain and constant stress respectively. The latter value is normally provided in the datasheets of piezoelectric materials. Also, C_e^T is the capacitance of the piezoelectric layers under constant stress, which is given by

$$C_e^T = 2\varepsilon_{33}^T\frac{bL}{h_{pe}}, \tag{22}$$

where b, L, h_{pe} are the width, length and thickness of the piezoelectric layers. As shown in Ref. [33], the lossy complex capacitance $\tilde{C}_e^S = C_e^S(1 - j\eta_c)$ can be modelled in terms of a capacitance and a resistance connected in parallel, such that $\tilde{C}_e^S =$

$C_e^S + \frac{G_e}{j\omega}$, where $G_e = \omega C_e^S \eta_C = 2\sigma_{pe}\frac{bL}{h_{pe}}$ is the conductance of the piezoelectric layers. To conclude, according to Ref. [33], the piezoelectric transduction coefficient ψ_{pe} is given by:

$$\psi_{pe} = e_{31} b z. \tag{23}$$

For the Euler–Bernoulli beam model the stress/charge constant is given by $e_{31} = Y_{pe}^E d_{31}$, and Y_{pe}^E, d_{31} are the material Young's modulus, assuming constant electric field, and the strain/charge constant [12]. Also, b is the width of the piezoelectric layers and $z = (h_s + h_{pe})\frac{\phi_1'(L)}{\phi_1(\bar{x})}$ is the distance between the piezoelectric layers mid-planes weighted by the ratio $\phi_1'(L)/\ \phi_1(\bar{x})$ between the slope and amplitude of the first flexural mode of the composite beam and tip mass assembly with the base mass clamped.

Tables A1 and A2 in Appendix A report the physical and geometrical properties of the reference electromagnetic and piezoelectric transducers that were thoroughly studied in Ref. [33]. The two transducers have approximately the same weight of ≈330 g, the same volume of ≈60 cm^3, and the same fundamental natural frequencies of ≈20 Hz. In this paper the scale L = 1 is thus referred to the characteristic dimension of the two prototypes, namely ≈4 cm .

2.2. Constitutive equations

The constitutive equations for the two transducers are set in the frequency domain with reference to the complex amplitude $f(\omega)$ of time-harmonic functions given in the form $f(t) = Re\{f(\omega)e^{j\omega t}\}$, where $j = \sqrt{-1}$ and ω is the circular frequency in [rad /s]. For simplicity, the frequency dependence of the complex functions is omitted throughout the paper. The electromechanical response of the electromagnetic and piezoelectric seismic harvesters are derived in terms of the following two-port network constitutive equations respectively:

$$\begin{bmatrix} f_h \\ e_h \end{bmatrix} = \begin{bmatrix} Z_{mi} & T_{fi} \\ T_{ew} & Z_{ei} \end{bmatrix} \begin{bmatrix} \dot{w}_h \\ i_h \end{bmatrix}, \tag{24}$$

$$\begin{bmatrix} f_h \\ i_h \end{bmatrix} = \begin{bmatrix} Z_{me} & T_{fe} \\ T_{iw} & Y_{ei} \end{bmatrix} \begin{bmatrix} \dot{w}_h \\ e_h \end{bmatrix}. \tag{25}$$

Here f_h, $\dot{w}_h$, e_h, i_h are the frequency-dependent complex amplitudes of the force and velocity at the base and the voltage across and current through the terminals of the seismic transducers. Also, T_{fi} and T_{ew} represent the electromechanical transduction Frequency Response Functions (FRFs) for the electromagnetic seismic transducer, which give the base force effect produced by the transducer per unit current flowing in the blocked seismic harvester, i.e. $T_{fi} = f_h/i_h|_{\dot{w}_h=0}$, and the electromotive force generated at the terminals of the transducer per unit velocity at the base of the open circuit seismic transducer, i.e. $T_{ew} = e_h/\dot{w}_h|_{i_h=0}$. Alternatively, T_{fe} and T_{iw} represent the electromechanical transduction FRFs for the piezoelectric seismic transducer, which provide the base force generated by the transducer per unit voltage imposed across the electric circuit in the blocked seismic transducer, i.e. $T_{fe} = f_h/e_h|_{\dot{w}_h=0}$, and the current generated per unit velocity at the base of the short circuited seismic transducer, i.e. $T_{iw} = i_h/\dot{w}_h|_{e_h=0}$. Finally, $Z_{ei} = e_h/i_h|_{\dot{w}_h=0}$ and $Y_{ei} = i_h/e_h|_{\dot{w}_h=0}$ are the output electrical impedance and admittance of the transducers blocked at their base, whereas $Z_{mi} = f_b/\dot{w}_h|_{i_h=0}$ and $Z_{me} = f_b/\dot{w}_h|_{e_h=0}$ are the input mechanical impedance of the open and short circuit transducers respectively.

The mechanical impedance, electrical impedance and the two electromechanical transduction FRFs for the electromagnetic transducer in Eq. (24) are given by the following expressions:

$$Z_{mi} = \left.\frac{f_h}{\dot{w}_h}\right|_{i_h=0} = Z_b + \frac{Z_s Z_m}{Z_t}, \tag{26}$$

$$T_{fi} = \left.\frac{f_h}{i_h}\right|_{\dot{w}_h=0} = \psi_{cm}\frac{Z_m}{Z_t}, \tag{27}$$

$$T_{ew} = \left.\frac{e_h}{\dot{w}_h}\right|_{i_h=0} = -\psi_{cm}\frac{Z_m}{Z_t}, \tag{28}$$

$$Z_{ei} = \left.\frac{e_h}{i_h}\right|_{\dot{w}_h=0} = Z_e + \frac{\psi_{cm}^2}{Z_t}, \tag{29}$$

where

$$Z_m = \mathrm{j}\omega m_m, \tag{30}$$

$$Z_b = \mathrm{j}\omega m_b, \tag{31}$$

$$Z_s = \frac{k_m}{\mathrm{j}\omega} + c_m, \tag{32}$$

$$Z_t = Z_s + Z_m = \frac{k_m}{\mathrm{j}\omega} + c_m + \mathrm{j}\omega m_m, \tag{33}$$

and m_b, m_m, k_m, c_m are given in Eqs. (1)–(4) respectively. Also, the electrical impedance for the electromagnetic transducer is given by:

$$Z_e = R_e + \mathrm{j}\omega\tilde{L}_e = R_e + \mathrm{j}\omega L_e^{'}(1 - \mathrm{j}\eta_L), \tag{34}$$

where R_e, $\tilde{L}_e$, $L_e^{'}$, η_L are given in Eqs. (7)–(10) respectively. Finally the transduction coefficient ψ_{cm} is given in Eq. (12).

Considering now the piezoelectric transducer, the mechanical impedance, electrical impedance and the two electromechanical transduction FRFs in Eq. (25) are given by the following expressions:

$$Z_{me} = \left.\frac{f_h}{\dot{w}_h}\right|_{e_h=0} = Z_b + \frac{Z_s Z_m}{Z_t}, \tag{35}$$

$$T_{fe} = \left.\frac{f_h}{e_h}\right|_{\dot{w}_h=0} = \psi_{pe}\frac{Z_m}{Z_t}, \tag{36}$$

$$T_{iw} = \left.\frac{i_h}{\dot{w}_h}\right|_{e_h=0} = -\psi_{pe}\frac{Z_m}{Z_t}, \tag{37}$$

$$Y_{ei} = \left.\frac{i_h}{e_h}\right|_{\dot{w}_h=0} = \frac{1}{Z_e} + \frac{\psi_{pe}^2}{Z_t}, \tag{38}$$

where

$$Z_m = \mathrm{j}\omega m_m + c_{am}, \tag{39}$$

$$Z_b = \mathrm{j}\omega m_b, \tag{40}$$

$$Z_s = \frac{k_m}{\mathrm{j}\omega} + c_m, \tag{41}$$

$$Z_t = Z_s + Z_m = \frac{k_m}{\mathrm{j}\omega} + c_m + c_{am} + \mathrm{j}\omega m_m, \tag{42}$$

and m_b, m_m, k_m, c_m, c_{am} are given in Eqs. (13), (14), (16)–(18) respectively. Also, the electrical impedance for the piezoelectric transducer is given by:

$$Z_e = \frac{1}{\mathrm{j}\omega\tilde{C}_e^s} = \frac{1}{\mathrm{j}\omega C_e^s(1 - j\eta_c)}, \tag{43}$$

where $\tilde{C}_e^s$, C_e^s, η_c are given in Eqs. (19)–(22) respectively. Finally, the transduction coefficient ψ_{pe} is given in Eq. (23).

The four plots in Fig. 2 show the modulus-phase diagrams of the four FRFs that characterise the electromechanical response of the electromagnetic seismic harvester. Plot (a) shows the typical base impedance FRF of a seismic electromagnetic transducer in open circuit, which is characterised by mass laws proportional to the total mass and to base mass of the transducer, respectively at low and high frequencies. Alternatively, between 10 Hz and 50 Hz, it is characterised by a resonance peak, in correspondence of the 20 Hz fundamental natural frequency of the transducer, and an antiresonance trough, at about 32 Hz, which are significantly smoothened by the Couette air damping and eddy currents damping effects. Plots (b) and

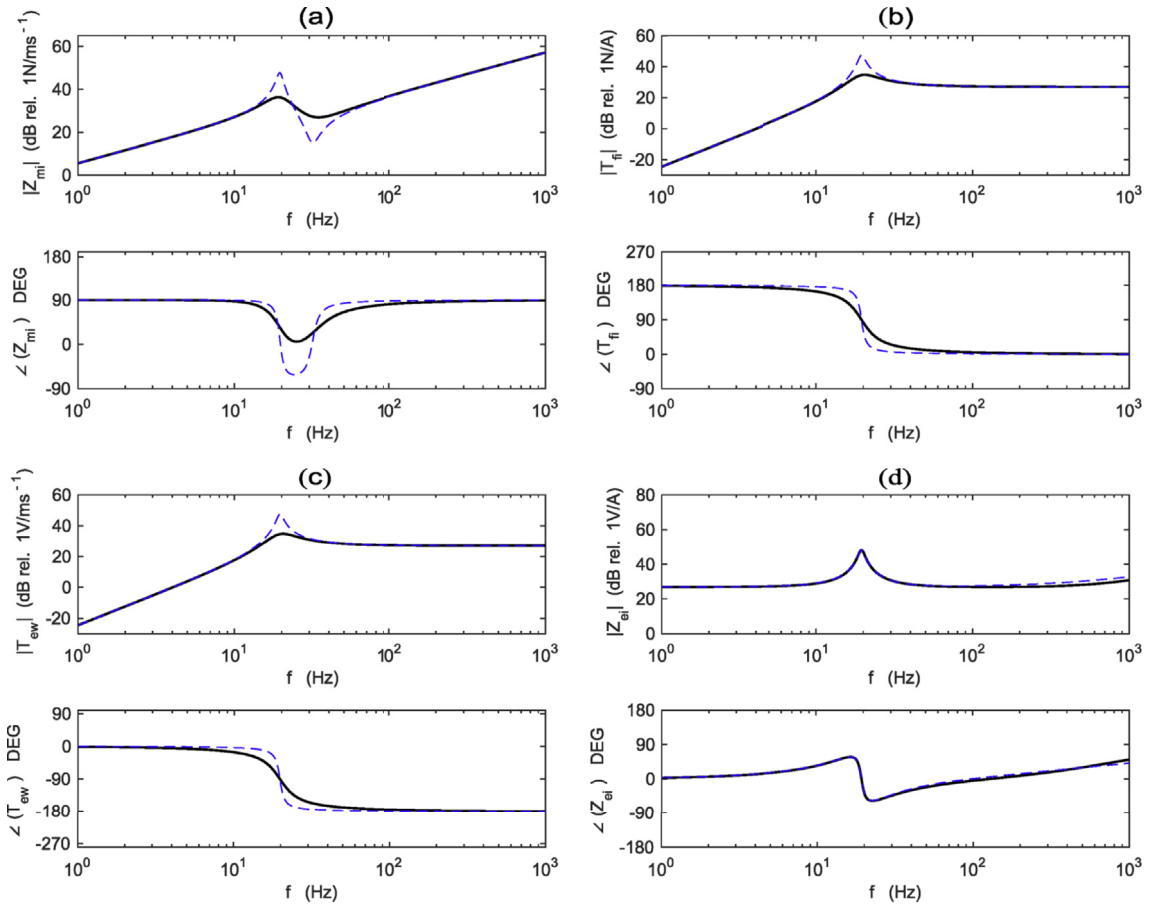

Fig. 2. Modulus-phase diagrams of the four characteristic FRFs for the electromagnetic seismic transducer introduced in Eq. (24) with (solid black line) and without (dashed blue line) eddy currents losses.

(c) show the two transduction FRFs, whose magnitude tends to increase proportionally to ω^2 up to the fundamental natural frequency, where it peaks, and then remains constant and equal to Bl_c. The phase shifts from $+180^o$ to 0^o and from 0^o to -180^o at frequencies close to the fundamental natural frequency. Again, the amplitude of the resonance peak is effectively smoothened by the Couette air damping and eddy currents damping effects. Finally, Plot (d) shows the typical electrical impedance function of a coil element, which is characterised by a low frequency resistive effect and, above the electrical cut-off frequency ω_{ce} at 805 Hz, a higher frequencies inductive effect. There is a peak at about the 20 Hz fundamental natural frequency of the transducer, which is due to the coupled electromechanical response of the transducer. The amplitude of this peak is also significantly smoothened by the Couette air damping and eddy currents damping effects. The inductive effect is characterised by the eddy current losses, which however grow exponentially with frequency, and thus become relevant only at higher frequencies, well above the fundamental natural frequency of the transducer at which the harvester is operating. Therefore, the energy formulation derived below considers a lossless inductance, i.e. $\tilde{L}_e = L_e$.

The four plots in Fig. 3 show the modulus-phase diagrams of the four FRFs that characterise the electromechanical response of the piezoelectric seismic harvester. Plot (a) shows a similar base impedance FRF to that found for the electromagnetic seismic harvester, which is therefore characterised by a low frequencies mass law (proportional to the transducer total mass), a resonance peak at about 20 Hz followed by an antiresonance trough at about 33 Hz and then a high frequencies mass law (proportional to the transducer base mass). The FRF is characterised by quite sharp resonance peak and anti-resonance trough, which are only slightly smoothened by the air damping effect. Plots (b) and (c) show the two transduction FRFs, which are also similar to those found for the electromagnetic transducer. Thus their magnitude rises proportionally to ω^2 up to the transducer fundamental natural frequency, where it peaks, and then remains constant and equal to $e_{31}bz$. Also, their phase starts respectively from 0^o and 180^o and shifts respectively to -180^o and 0^o in correspondence to the transducer fundamental natural frequency. At last, Plot (d) shows the electrical admittance function, which is dominated by the capacitive effect of the piezoelectric layers. Indeed, the mechanical response of the transducer produces only a small glimpse at the 20 Hz fundamental natural frequency of the transducer.

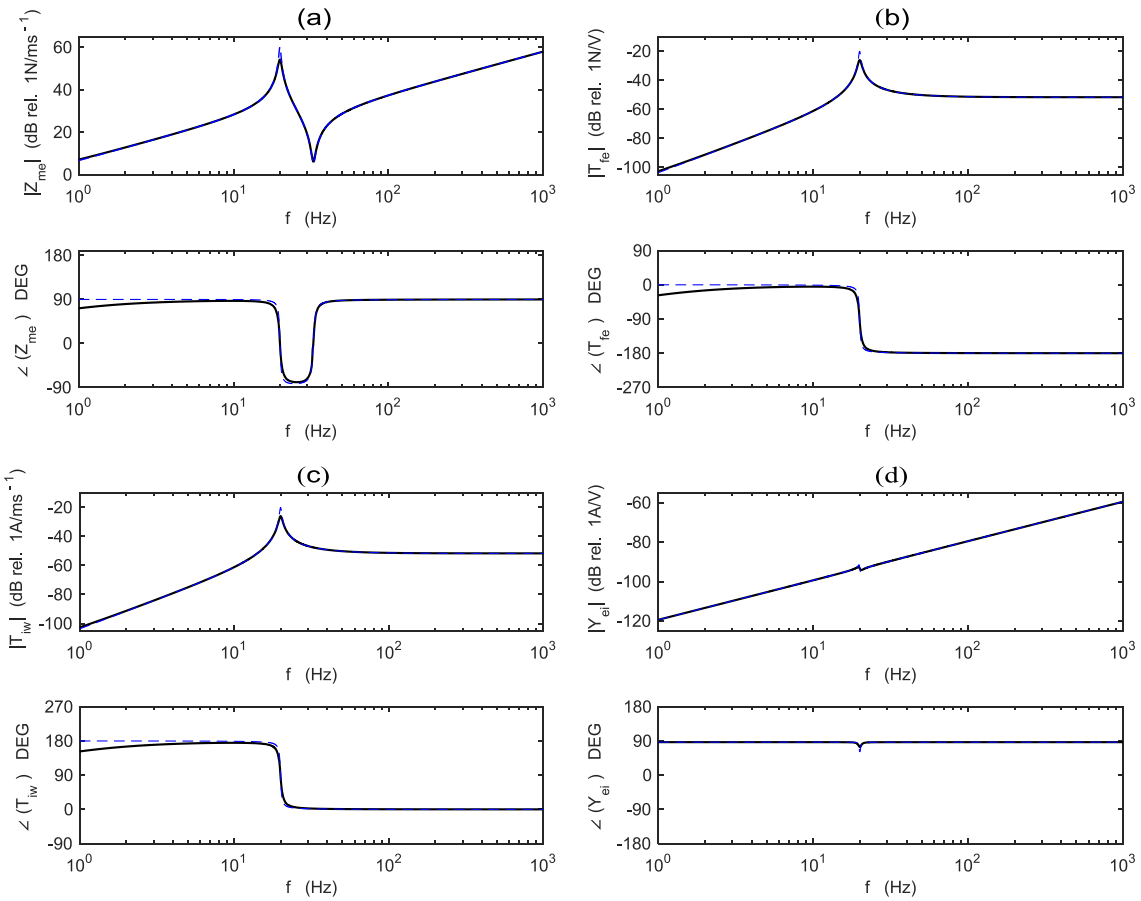

Fig. 3. Modulus-phase diagrams of the four characteristic FRFs for the piezoelectric seismic transducer introduced in Eq. (25) with (solid black line) and without (dashed blue line) air damping. (For interpretation of the references to colour in this figure legend, the reader is referred to the Web version of this article.)

2.3. Power transduction factors

In this paper, the power transmission effects occurring in the electromechanical and piezoelectric transducers are investigated considering time-harmonic base vibrations at the fundamental natural frequency of the transducers. To provide neat mathematical formulations that separate the intrinsic power transmission propertied for the electromagnetic and piezoelectric transductions from the physical effects produced by the second order mechanical responses and first order electrical responses of the seismic transducers, the so called *power transduction factors* are first introduced in this section. To this end, as shown in the sketches (a) and (c) of Fig. 4, the seismic components of the two transducers are assumed clamped. Also, since the focus is on the power transmission, as shown in the lumped parameter models (b) and (d), the inertia and stiffness mechanical effects as well as the inductive and capacitive electrical effects in the two transducers are not taken into consideration.

The analysis considers the time-averaged total power input into the two transducers, which, for harmonic vibrations can be derived from the following relation:

$$\overline{P} = \frac{1}{T}\int_0^T P(\mathrm{t})dt. \tag{44}$$

Here $T = \frac{2\pi}{\omega_n}$ is the time period of the harmonic vibration and $P(\mathrm{t})$ is the instantaneous power injected into the transducers, which is given by:

$$P(\mathrm{t}) = f_h(t)\dot{w}_h(\mathrm{t}) + i_h(t)e_h(t) \tag{45}$$

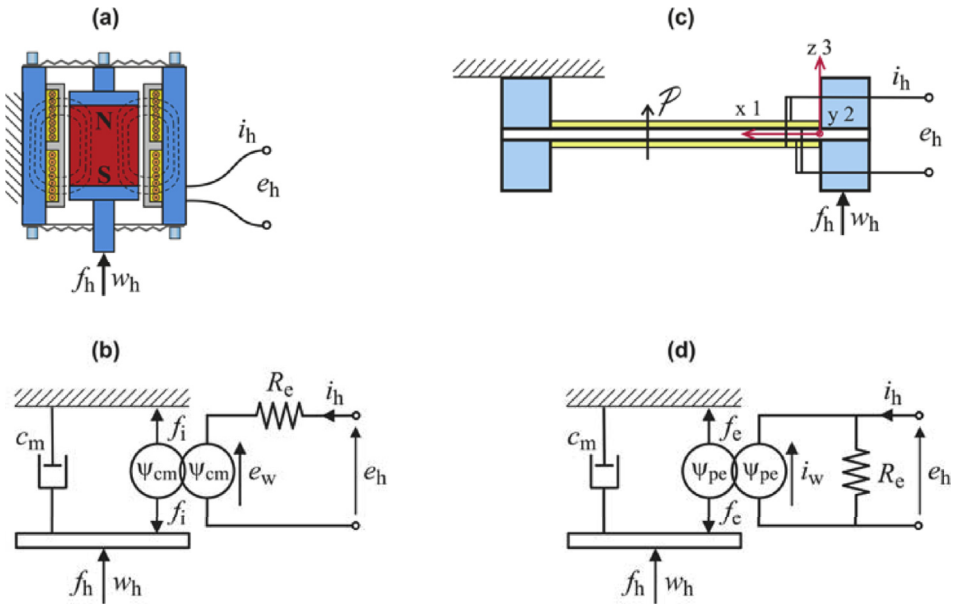

Fig. 4. Sketches (a,c) and lumped parameter schematics (b,d), of the electromagnetic (left hand side) and piezoelectric (right hand side) seismic transducers considered for the derivation of the power transduction factors.

2.3.1. Electromagnetic harvester

The constitutive equations for the electromagnetic transducer shown in the sketch a of Fig. 4 can be readily derived by inspection of the lumped parameter model b:

$$\begin{bmatrix} f_h \\ e_h \end{bmatrix} = \begin{bmatrix} c_m & -Bl_c \\ Bl_c & R_e \end{bmatrix} \begin{bmatrix} \dot{w}_h \\ i_h \end{bmatrix}. \tag{46}$$

To derive the total input power defined in Eq. (45), the expression above is rewritten in the following form that considers $\dot{w}_h$ and e_h as independent variables:

$$\begin{bmatrix} f_h \\ i_h \end{bmatrix} = \begin{bmatrix} c_m\left(1+\dfrac{(Bl_c)^2}{c_m R_e}\right) & -\dfrac{Bl_c}{R_e} \\ -\dfrac{Bl_c}{R_e} & \dfrac{1}{R_e} \end{bmatrix} \begin{bmatrix} \dot{w}_h \\ e_h \end{bmatrix}. \tag{47}$$

Substituting the expressions for the variables f_h and i_h given above into Eq. (45) and then into Eq. (44), the time-averaged total power input into the transducer results given by:

$$\overline{P} = \overline{P}_{MM} + \overline{P}_{EE} + \overline{P}_{ME} + \overline{P}_{EM} = \frac{1}{2}c_m\left(1+\frac{\psi_{cm}^2}{c_m R_e}\right)\dot{w}_h^2 + \frac{1}{2}\frac{1}{R_e}e_h^2 - \frac{1}{2}\frac{\psi_{cm}}{R_e}\dot{w}_h e_h - \frac{1}{2}\frac{\psi_{cm}}{R_e}e_h\dot{w}_h. \tag{48}$$

This expression is composed by four terms, which correspond to: a) the mechanical input power $\overline{P}_{MM} = \frac{1}{2}c_m\left(1+\frac{\psi_{cm}^2}{c_m R_e}\right)\dot{w}_h^2$ when the transducer is in short circuit, i.e. $e_h = 0$; b) the electrical input power $\overline{P}_{EE} = \frac{1}{2}\frac{1}{R_e}e_h^2$ when the transducer is blocked, i.e. $\dot{w}_h = 0$; c) the mechanical to electrical power transmission $\overline{P}_{ME} = -\frac{1}{2}\frac{\psi_{cm}}{R_e}\dot{w}_h e_h$; and d) the electrical to mechanical power transfer $\overline{P}_{EM} = -\frac{1}{2}\frac{\psi_{cm}}{R_e}e_h\dot{w}_h$. At this point, in analogy to what is normally done for the energy coupling factors of transducers (e.g. see Ref. [62]), the following power transduction factor is defined

$$\Pi_{cm}^2 = \frac{P_{ME}P_{EM}}{P_{MM}P_{EE}} = \frac{\frac{\psi_{cm}^2}{c_m R_e}}{1+\frac{\psi_{cm}^2}{c_m R_e}}. \tag{49}$$

This factor provides a figure of merit for the characteristic power transmissions, mechanical to electrical and vice versa, with respect to the input mechanical and electrical powers of the electromagnetic transducer. More specifically it can be seen as the geometric average of the power transmission, mechanical to electrical and vice versa, with respect to the geometric average of the power input.

2.3.2. Piezoelectric harvester

Analogously to the electromagnetic transducer, the power transduction factor for the piezoelectric transducer can be derived from the constitutive equations of the lumped parameter model depicted in the scheme of Fig. 4 (d):

$$\begin{bmatrix} f_h \\ i_h \end{bmatrix} = \begin{bmatrix} c_m & -\psi_{pe} \\ \psi_{pe} & G_e \end{bmatrix} \begin{bmatrix} \dot{w}_h \\ e_h \end{bmatrix}. \tag{50}$$

Assuming voltage controlled transducer the electrical independent variables i_h and e_h can be interchanged. Thus Eq. (50) can be rewritten as:

$$\begin{bmatrix} f_h \\ e_h \end{bmatrix} = \begin{bmatrix} c_m\left(1+\frac{\psi_{pe}^2}{c_m G_e}\right) & -\frac{\psi_{pe}}{G_e} \\ -\frac{\psi_{pe}}{G_e} & \frac{1}{G_e} \end{bmatrix} \begin{bmatrix} \dot{w}_h \\ i_h \end{bmatrix}. \tag{51}$$

As done for the electromagnetic transducer, substituting the expressions for the variables f_h and i_h given above into Eq. (45) and then into Eq. (44), the time-averaged total power input into the transducer results given by:

$$\overline{P} = \overline{P}_{MM} + \overline{P}_{EE} + \overline{P}_{ME} + \overline{P}_{EM} = \frac{1}{2}c_m\left(1+\frac{\psi_{pe}^2}{c_m G_e}\right)\dot{w}_h^2 + \frac{1}{2}\frac{1}{G_e}i_h^2 - \frac{1}{2}\frac{\psi_{pe}}{G_e}\dot{w}_h i_h - \frac{1}{2}\frac{\psi_{pe}}{G_e}i_h\dot{w}_h. \tag{52}$$

The first term $\overline{P}_{MM} = \frac{1}{2}c_m\left(1+\frac{\psi_{pe}^2}{c_m G_e}\right)\dot{w}_h^2$ can be identified as the mechanical power dissipated in the damper in open circuit condition i.e. $i_h = 0$; $\overline{P}_{EE} = \frac{1}{2}\frac{1}{G_e}i_h^2$ is the electrical power lost in the resistance assuming blocked moving mass i.e. $\dot{w}_h = 0$. Finally, the term $\overline{P}_{ME} = -\frac{1}{2}\frac{\psi_{pe}}{G_e}\dot{w}_h i_h$ is the mechanical to electrical power transmission while $\overline{P}_{EM} = -\frac{1}{2}\frac{\psi_{pe}}{G_e}i_h\dot{w}_h$ is the electrical to mechanical power transmission. Similarly to the electromagnet device, the power transduction factor Π_{pe}^2 is thus defined as follows:

$$\Pi_{pe}^2 = \frac{P_{ME}P_{EM}}{P_{MM}P_{EE}} = \frac{\frac{\psi_{pe}^2}{c_m G_e}}{1+\frac{\psi_{pe}^2}{c_m G_e}}. \tag{53}$$

Again, this factor provides a figure of merit for the characteristic power transmissions, mechanical to electrical and vice versa, with respect to the input mechanical and electrical powers of the piezoelectric transducer.

3. Electromagnetic harvester: scaling study

The scaling laws for the physical and energy harvesting properties of the electromagnetic seismic harvester are first addressed in this section. To start with, the characteristic energy expressions are derived considering the harvester is connected to the optimal complex and purely real harvesting loads. Then, the scaling laws of the principal mechanical and electrical physical properties that characterise the harvester are thoroughly revised. Finally, the scaling of the harvested power and the scaling of the power efficiency are systematically investigated assuming the harvester is excited at its fundamental natural frequency, i.e. ω_n, such that, as shown in Appendix B.1, the maximum power is harvested.

3.1. Energy formulation

Considering first the harvested power, according to the sign convention used in the lumped parameter model shown in Fig. 1b, the following relation holds for the voltage e_h at the terminals of the harvesting electrical load having impedance Z_h:

$$e_h = -Z_h i_h. \tag{54}$$

Substituting this equation into the matrix expression in Eq. (24) the following relation is derived:

$$i_h = -\frac{T_{ew}}{Z_{ei}+Z_h}\dot{w}_h. \tag{55}$$

Thus, the time-averaged harvested power (for brevity harvested power from here on) results:

$$\overline{P}_h = \frac{1}{2}\mathrm{Re}\{Z_h\}|i_h|^2 = \frac{1}{2}\mathrm{Re}\{Z_h\}\left|-\frac{T_{ew}}{Z_{ei}+Z_h}\right|^2|\dot{w}_h|^2. \tag{56}$$

As shown in Ref. [33], according to the Fermat's theorem [63], the complex electric load Z_h, which maximizes the harvested power at each frequency, is given by:

$$Z_{h,opt} = Z_{ei}^*, \tag{57}$$

where * denotes the complex conjugate. Alternatively, if Z_h is assumed purely real, the optimal electric load is given by Ref. [33]:

$$Z_{hR,opt} = |Z_{ei}|. \tag{58}$$

Therefore, substituting Eqs. (57) and (58) into Eq. (56), the harvested power for the complex and real optimal loads are derived as follows:

$$\overline{P}_h = \frac{1}{8}\frac{|T_{ew}|^2}{\mathrm{Re}\{Z_{ei}\}}|\dot{w}_h|^2, \tag{59}$$

$$\overline{P}_{hR} = \frac{1}{4}\frac{|T_{ew}|^2}{|Z_{ei}|+\mathrm{Re}\{Z_{ei}\}}|\dot{w}_h|^2. \tag{60}$$

Setting $\omega = \omega_n$ in Eqs. (59) and (60), the maximum power harvested with the complex and real optimal loads results given by:

$$\overline{P}_h = \frac{1}{8}\frac{k_m m_m}{c_m}\Pi_{cm}^2|\dot{w}_h|^2, \tag{61}$$

$$\overline{P}_{hR} = \frac{1}{8}\frac{k_m m_m}{c_m}\frac{\Pi_{cm}^2}{\alpha_{cm}}|\dot{w}_h|^2, \tag{62}$$

where Π_{cm}^2 is the power transduction factor defined in Eq. (49). Also,

$$\alpha_{cm} = \frac{1+\sqrt{1+\beta_{cm}^2}}{2}, \tag{63}$$

where $\beta_{cm} = \frac{\omega_n}{\omega_{ce}}(1-\Pi_{cm}^2)$. Here, $\omega_n = \sqrt{k_m/m_m}$ is the transducer fundamental natural frequency and $\omega_{ce} = R_e/L_e$ is the cut-off frequency where the coil electric impedance switches from resistive to inductive types.

Moving now to the input power, substituting in Eq. (24) the expression for the current i_h derived in Eq. (55), the following mechanical base impedance of the transducer can be derived:

$$Z_{mh} = Z_{mi} - \frac{T_{ew}T_{fi}}{Z_{ei}+Z_h}. \tag{64}$$

Thus, the time-averaged input power (for brevity, input power from here on) results:

$$\overline{P}_i = \lim_{T\to\infty}\frac{1}{T}\int_0^T P_i(t)\mathrm{d}t = \frac{1}{2}\mathrm{Re}\{Z_{mh}\}|\dot{w}_h|^2 = \frac{1}{2}\mathrm{Re}\left\{Z_{mi} - \frac{T_{ew}T_{fi}}{Z_{ei}+Z_h}\right\}|\dot{w}_h|^2. \tag{65}$$

Substituting Eqs. (57) and (58) in this equation, the input power for the complex and real optimal loads result:

$$\overline{P}_i = \frac{1}{2}\mathrm{Re}\left\{Z_{mi} - \frac{T_{ew}T_{fi}}{2\mathrm{Re}\{Z_{ei}\}}\right\}|\dot{w}_h|^2, \tag{66}$$

$$\overline{P}_{iR} = \frac{1}{2}\mathrm{Re}\left\{Z_{mi} - \frac{T_{ew}T_{fi}}{Z_{ei}+|Z_{ei}|}\right\}|\dot{w}_h|^2. \tag{67}$$

Considering $\omega = \omega_n$, the two equations above reduce to the following expressions respectively for the optimal complex $Z_{h,opt}$ and purely real $Z_{hR,opt}$ harvester loads:

$$\overline{P}_i = \frac{1}{4}\frac{k_m m_m}{c_m}\left(2 - \Pi_{cm}^2\right)|\dot{w}_h|^2, \tag{68}$$

$$\overline{P}_{iR} = \frac{1}{4}\frac{k_m m_m}{c_m}\left(2 - \frac{4\alpha_{cm}}{4\alpha_{cm}^2+\beta_{cm}^2}\Pi_{cm}^2\right)|\dot{w}_h|^2\ . \tag{69}$$

The power harvesting efficiency E, defined as the ratio between the harvested and input time-average powers,

$$E = \frac{\overline{P}_h}{\overline{P}_i}, \tag{70}$$

can now be derived using Eqs. (56) and (65):

$$E = \frac{\left|\mathrm{Re}\{Z_h\} - \frac{T_{ew}}{Z_{ei}+Z_h}\right|^2}{\mathrm{Re}\left\{Z_{mi} - \frac{T_{ew}T_{fi}}{Z_{ei}+Z_h}\right\}}. \tag{71}$$

Considering the optimal complex and real impedances, $Z_{h,opt} = Z_{ei}^*$ and $Z_{hR,opt} = |Z_{ei}|$, the above expression becomes respectively:

$$E = \frac{1}{4}\frac{|T_{ew}|^2}{\mathrm{Re}\{Z_{ei}\}\mathrm{Re}\left\{Z_{mi} - \frac{T_{ew}T_{fi}}{2\mathrm{Re}\{Z_{ei}\}}\right\}}, \tag{72}$$

$$E_R = \frac{1}{2}\frac{\frac{|T_{ew}|^2}{|Z_{ei}|+\mathrm{Re}\{Z_{ei}\}}}{\mathrm{Re}\left\{Z_{mi} - \frac{T_{ew}T_{fi}}{Z_{ei}+|Z_{ei}|}\right\}}. \tag{73}$$

Thus, assuming $\omega = \omega_n$,

$$E = \frac{1}{2}\frac{\Pi_{cm}^2}{2-\Pi_{cm}^2}, \tag{74}$$

$$E_R = \frac{1}{2}\frac{\Pi_{cm}^2\left(4\alpha_{cm}^2+\beta_{cm}^2\right)}{2\alpha_{cm}\left(4\alpha_{cm}^2+\beta_{cm}^2-2\alpha_{cm}\Pi_{cm}^2\right)}, \tag{75}$$

respectively for optimal complex and purely real harvesting loads.

3.2. Scaling laws of the lumped parameter elements

The scaling laws of the lumped parameter elements that compose the electromagnetic transducer shown in Fig. 1a are first revised in this section. The scaling laws can be readily derived recalling that the physical properties of the transducer components (e.g. density, Young's modulus of elasticity, resistivity, magnetic flux density) do not vary with scale. For instance, according to Eq. (2), the mass of the ferromagnetic ring and coil assembly m_m is proportional to the densities (ρ_r, ρ_c) and volumes (V_r, V_c) of the two components, thus it scales proportionally to the cube of the dimension, i.e. $[L^3]$. Also, the bending stiffness k_m of the spiral springs [37] given in Eq. (3) is proportional to the material Young's modulus of elasticity, E_k, and to the ratio between the cross section area, A_k, and the length of the spirals, h_k, such that it scales proportionally to dimension, i.e. $[L^1]$. According to Eq. (12), the transduction coefficient, $\psi_{cm} = Bl_c$, is proportional to the magnetic flux density, B, and to the length of the coil winding, l_c [27,37]; thus it scales proportionally with dimension, i.e. $[L^1]$. The electrical resistance R_e of the coil wire given in Eq. (7) is proportional to the resistivity, ρ_e, and length, l_r, of the wire and inversely proportional to the cross section of the wire, A_r; thus it scales proportionally to the inverse of dimension, i.e. $[L^{-1}]$. Also, since the magnetic permeability μ_e is a property of the material and assuming that the number N of the coil turns does not vary with the dimension [40], it follows that the inductance given in Eq. (11) varies linearly with the dimension size of the transducer, i.e. $[L^1]$. According to Eq. (5), the Couette air damping is proportional to the fluid viscosity μ_c and to the lateral surface of the magnetic cylinder A_c and is inversely proportional to the radial gap between the inner magnetic cylinder and the outer coil and ferromagnetic ring d_c. Therefore, the Couette air damping coefficient scales proportionally to $[L^1]$. Numerical simulations have been performed in order to evaluate how the eddy currents damping coefficient c_{ec} scales with reference to the device characteristic dimension. The result shows that the radial magnetic field density B_r generated by the inner permanent magnet does not increase in value with the dimension of the device, provided the magnet maintains the same aspect ratio; i.e. the magnitude of the field remains constant, whereas the field gradient ∇B_r increases if the dimension is reduced ([40,53]). As a result, it can be proved that c_{ec} scales with the volume of the transducer and thus as the cube of the characteristic length, i.e. $[L^3]$. However, the presence of the diffusion phenomenon, due to the interaction of the eddy currents with the magnetic field generated by the inner cylindrical magnet, produces an exponential reduction in the distribution of the current density along the radial direction of the outer ferromagnetic ring. In this case, the eddy currents damping coefficient c_{ec} is given by the expression derived in Eq. (6). Therefore, if the electromagnetic harvester works at its natural frequency ω_n, the skin depth can be specified as $\delta = \sqrt{\frac{2}{\omega_n \mu_e \sigma_{pe}}}$, which implies that δ scales as $[L^{0.5}]$ since μ_e and σ_{pe} are properties of the material and $\omega_n = \sqrt{k_m/m_m}$ scales inversely proportional to the dimension, i.e. $[L^{-1}]$. As a result the damping coefficient c_{ec} varies proportionally to $[L^{2.5}]$. Thus, for small scale harvesters, damping is mainly due to the Couette airflow between the coil and inner cylindrical magnet, whereas, for large scale harvesters, damping is principally controlled by the eddy currents losses that arise in the ferromagnetic outer ring.

In summary, as shown in Plot a of Fig. 5, as the size of the transducer is scaled up, the electric resistance R_e tends to decrease as $[L^{-1}]$, while the spring stiffness k_m, the Couette air damping coefficient c_a, the electric inductance L_e and the electromagnetic transduction coefficient ψ_{cm} rise proportionally to $[L^1]$. Also, the eddy currents damping c_{ec} scales as $[L^{2.5}]$, whereas the moving mass of the transducer m_m scales proportionally to $[L^3]$. Therefore, as shown in Plot b of Fig. 5, the

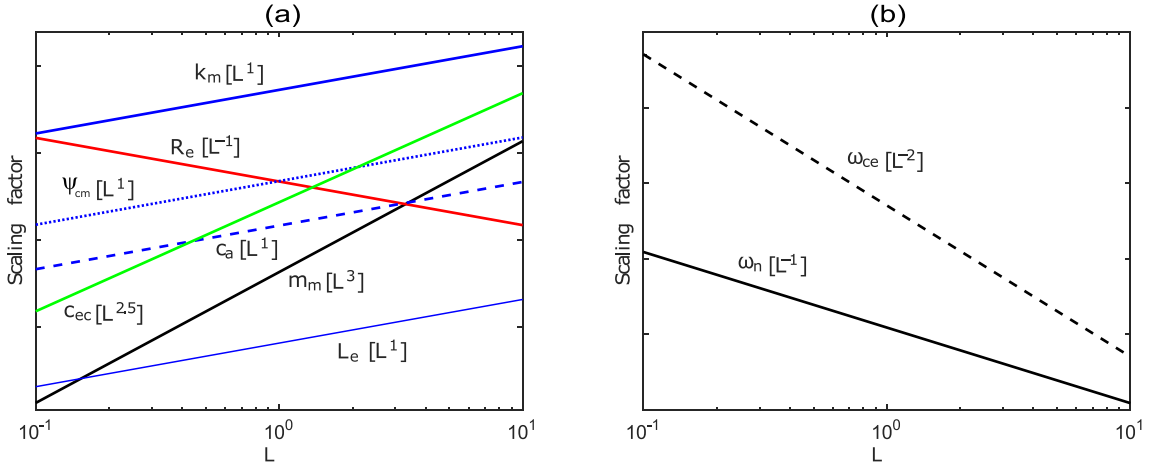

Fig. 5. (a) Scaling laws for the moving mass m_m (black solid line), the stiffness k_m (blue solid line), the Couette air film damping coefficient c_a (blue dashed line) and eddy current damping c_{ec} (green solid line), the electrical resistance R_e (red solid line), the inductance L_e (blue thin solid line) and the transduction coefficient ψ_{cm} (blue dotted line). (b) Scaling laws for the mechanical natural frequency ω_n (solid line) and the electrical cut-off frequency ω_{ce} (dashed line). (For interpretation of the references to colour in this figure legend, the reader is referred to the Web version of this article.)

fundamental natural frequency of the transducer, $\omega_n = \sqrt{k_m/m_m}$, scales with $[L^{-1}]$, whereas the electrical cut-off frequency $\omega_{ce} = R_e/L_e$ scales proportionally to $[L^{-2}]$. Thus, in principle, for large transducers the fundamental natural frequency may be higher than the electrical cut-off frequency, i.e. $\frac{\omega_n}{\omega_{ce}} > 1$. Nevertheless, Plot b clearly indicates that this would occur for very large transducers with characteristic dimension well outside the practical range considered in this study (e.g. characteristic dimensions greater than 168cm).

The power expressions derived in Section 3.1 are based on the so called electromagnetic power transduction factor Π^2_{cm}, which, as shown in Section 2.3.1, gives the ratio of the power transfer within the transducer per input power to the transducer. According to Eq. (49) this factor depends on: a) the square of the transduction coefficient $\psi^2_{cm} = (Bl_c)^2$, b) the damping factor $c_m = c_a + c_{ec}$ and c) the coil resistance R_e. These parameters scale respectively proportionally to a) $[L^2]$, b) either $[L^1]$ (small size) or $[L^{2.5}]$ (large size) and c) $[L^{-1}]$. As shown in Fig. 6, the resulting scaling law is characterised by two asymptotes: for small dimensions, it scales proportionally to $[L^2]$ whereas, for large dimensions, it tends to a constant value, that is it scales proportionally to $[L^0]$. The energy harvesting with a real harvesting impedance load also depends on the $\alpha_{cm} = \frac{1+\sqrt{1+\beta^2_{cm}}}{2}$ factor defined in Eq. (63). As shown in Fig. 5b, for the range of dimensions considered in this study, the cut-off frequency where the electric impedance switches from resistive to inductive, is much greater than the mechanical fundamental natural frequency, that is $\omega_{ce} \gg \omega_n$. Therefore, the electric impedance of the transducer is controlled by the resistive effect. As a result the coefficient $\beta_{cm} = \frac{\omega_n}{\omega_{ce}}(1 - \Pi^2_{cm})$ tends to 0 and α_{cm} is approximately equal to 2, i.e. it scales proportionally to $[L^0]$. Therefore, considering the power and efficiency expressions derived in Section 3.1, for practical harvesters, the harvested and input powers and the efficiency with the optimal real and complex harvesting loads are about the same, that is: a) $\overline{P}_h \cong \overline{P}_{hR} \cong \frac{1}{8}\frac{k_m m_m}{c_m}\Pi^2_{cm}|\dot{w}_h|^2$, b) $\overline{P}_{iR} \cong \overline{P}_i \cong \frac{1}{4}\frac{k_m m_m}{c_m}(2 - \Pi^2_{cm})|\dot{w}_h|^2$, c) $E_R \cong E \cong \frac{1}{2}\frac{\Pi^2_{cm}}{2-\Pi^2_{cm}}$. If the transducer were built with exceptionally large dimensions grater than 168 cm, the cut-off frequency where the electric impedance switches from resistive to inductive would be smaller than the mechanical fundamental natural frequency, that is $\omega_{ce} \ll \omega_n$. In this case, the electric impedance of the transducer would show an inductive effect in correspondence to the mechanical fundamental natural frequency and thus α_{cm} whould scale proportionally to $[L^1]$ so that the harvested and input power and the efficiency with the optimal real load would be smaller than with the complex harvesting load. This would be because the real harvesting load cannot compensate the inductive effect of the coil and thus part of the energy absorbed by the transducer would be stored in the coil rather than transferred to the harvesting load.

3.3. Scaling laws of the normalised power density and efficiency

The scaling laws for the normalised harvested power density and for the power harvesting efficiency are now examined. The normalised harvested power density $\overline{\overline{P_h}} = \frac{\overline{P}_h}{V_h}\Big|_{\dot{w}=1g}$ is given by the time-averaged harvested power $\overline{P}_h$ per unit volume of the transducer V_h, assuming 1g base acceleration at $\omega = \omega_n$. The 1g base acceleration is assumed independently from the transducer scale. This implies that the mechanical characteristic impedance of the source of vibration is much greater than the mechanical base impedance of the harvester in the whole scale range. In other words, the source of vibration is assumed

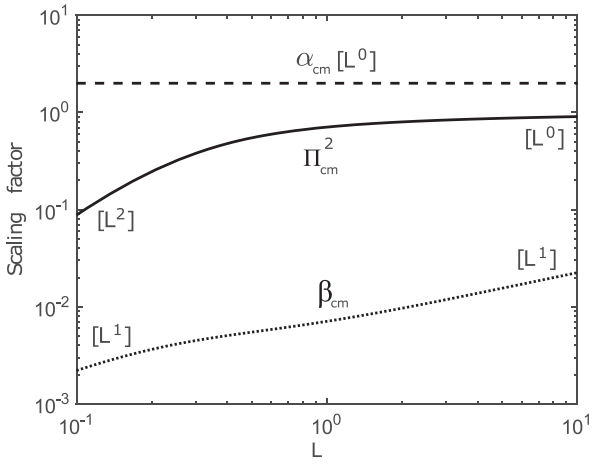

Fig. 6. Scaling laws of the electromagnetic power transduction factor Π^2_{cm} (solid line), the inductance effect coefficient α_{cm} (dashed line) and the β_{cm} coefficient (dotted line).

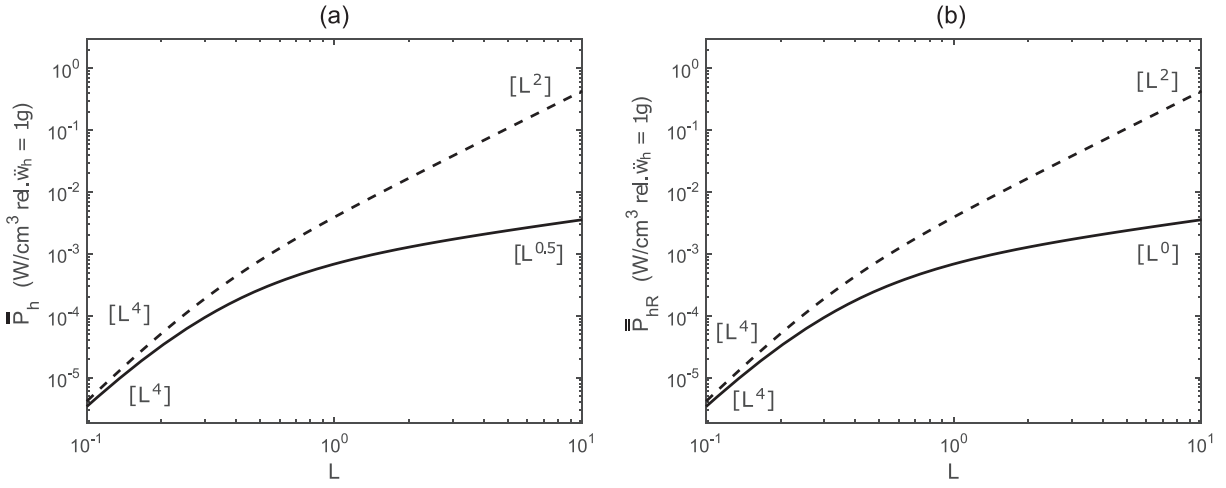

Fig. 7. Scaling laws of the normalised harvested power density $\overline{\overline{P_h}}$ when (a) the optimal complex and (b) optimal purely real electrical loads are implemented and the electromagnetic transducer is (solid line) or is not (dashed line) affected by eddy currents damping.

much larger than the harvester in the whole scale range considered in this study. The scaling laws were derived numerically from Eqs. (61), (62) and (74), (75) considering the scaling of the lumped elements shown in Figs. 5 and 6.

Fig. 7 shows the scaling laws of the normalised power density when the optimal complex, Plot a, and purely real, Plot b, harvesting loads are implemented. Considering first Plot a for the optimal complex electric load, the solid line shows that the harvested power monotonically rises as the scale of the harvester is increased. More specifically, the scaling law is characterised by two asymptotes with respect to the 4cm reference harvester choses in this study: for small dimensions, it scales proportionally to $[L^4]$ whereas, for large dimensions, it scales proportionally to $[L^{0.5}]$. If the effect of eddy currents in the ferromagnetic ring were removed, then, according to the dashed line, for large dimensions of the transducer, the harvested power would rise proportionally to $[L^2]$ instead of $[L^{0.5}]$. Moving to Plot b for the optimal real (i.e. resistive) electric load, the solid and dashed lines show very similar scaling laws as those depicted in Plot a for the harvester with the optimal complex electric load. In fact, with respect to the reference dimension 4cm, the harvested power of small harvesters scales proportionally to $[L^4]$, whereas for large harvesters it scales proportionally either to $[L^0]$ or $[L^2]$ depending on whether the outer ring is or is not affected by eddy currents that further dampen the response of the harvester.

Comparing Plots a and b, it can be noted that, for large transducers affected by eddy currents, the harvested power with the optimal real load scales proportionally to $[L^{0.5}]$ whereas with the optimal complex load scales proportionally to $[L^0]$. This small difference is probably due to the fact that the electrical cut-off frequency of large scale harvesters gets closer to their fundamental natural frequency so that the electromechanical response of the transducer at its fundamental natural frequency is affected more by the coil inductance. Overall, this results into a slightly smaller exponential factor for the scaling law. In summary, contrasting the two plots in Fig. 7, it can be noticed that, as anticipated in Section 3.2, the complex and real harvesting loads produce very similar levels of harvested power in the whole scaling range. This is due to the fact that, for the range of scales considered in this study, the electric response of the coil is primarily resistive and thus little difference is produced when a complex load is implemented to compensate the inductive electrical effect of the coil. Also, the scaling plots shown in Fig. 7 suggest that the harvested power tends to grow at a greater rate than the volume of the harvester. Therefore, the electromagnetic transduction is better suited for the construction of large scale harvesters. However, special care should be taken in the design stage to avoid eddy currents develops in the ferromagnetic components, which would greatly increase the effect of damping and weaken the amount of power that can be harvested.

Moving to the efficiency analysis, Fig. 8 shows how the effectiveness to absorb power from ambient imposed vibrations varies with the dimension of the electromagnetic harvester when the optimal complex (Plot a) and the optimal real (Plot b) electric loads are implemented. The solid lines in the two plots show that the efficiency scales with very similar "S-type" laws for the two types of harvesting loads, which for small dimensions tend to zero and for large dimensions tend to 0.5. Also, the dashed lines in the two plots indicate that, when the transducer is not affected by eddy currents damping, the transitions to the maximum 0.5 efficiency occurs at smaller scales.

Considering first the case where the optimal complex harvesting load $Z_{h,opt}$ is implemented, according to Eq. (74), the energy harvesting efficiency solely depends on the electromagnetic power transduction factor Π^2_{em}. In-depth analysis of Eq. (74) and of the scaling plot for Π^2_{em} shown in Fig. 6 indicates that, indeed, for small dimensions of the transducer, only a small amount of the input power can be converted into harvested power. Instead, for large dimensions of the transducer, a maximum of 50% of the input power can be converted into harvested power. Thus, the "S-type" scaling law arises from

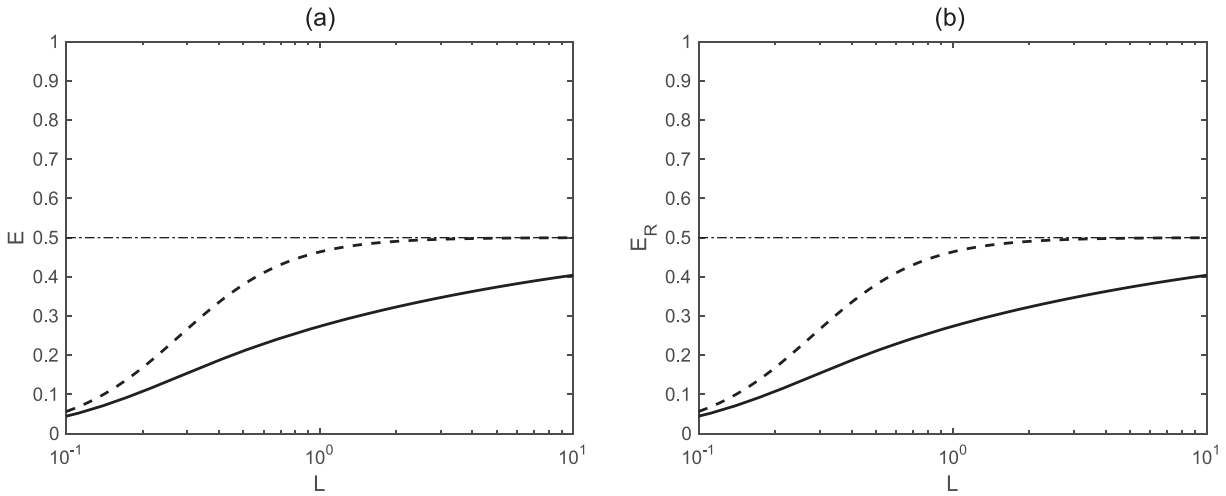

Fig. 8. Scaling laws of the power harvesting efficiency when (a) the optimal complex and (b) optimal purely real electrical loads are implemented and the electromagnetic transducer is (solid line) or is not (dashed line) affected by eddy currents damping.

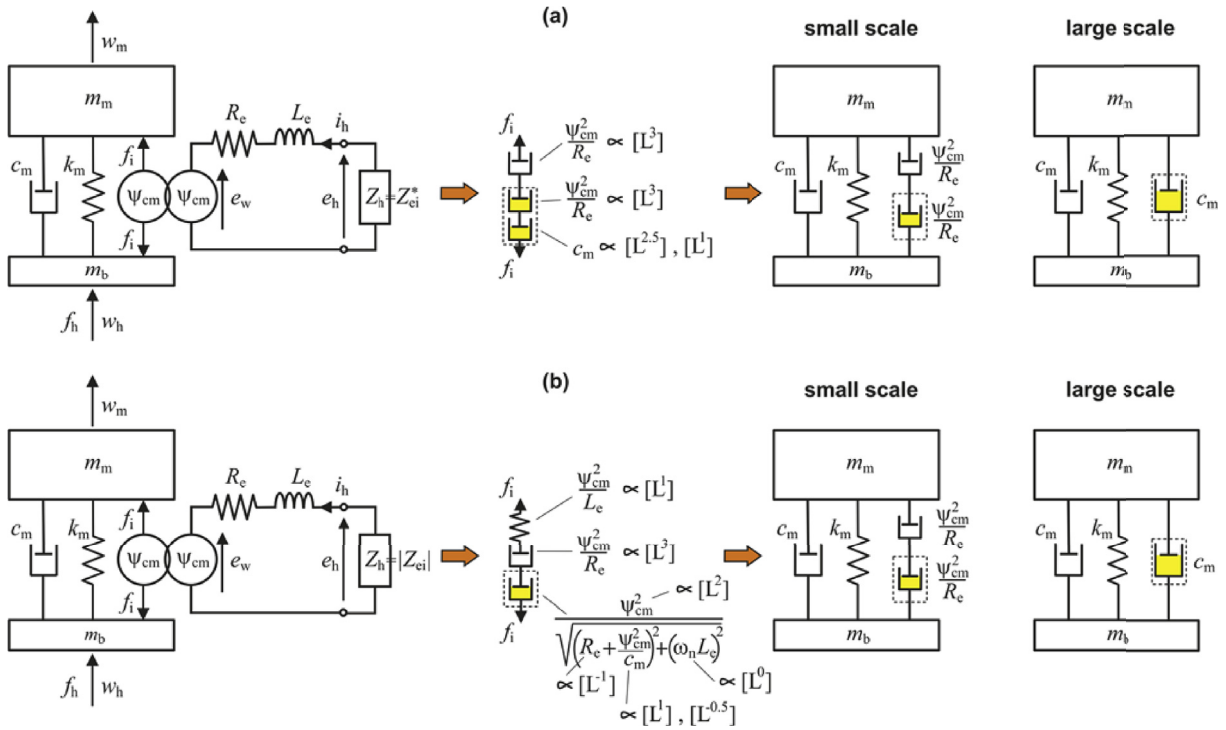

Fig. 9. Sketches of the equivalent mechanical effects produced by the electrical components of small scale and large scale electromagnetic harvesters with optimal complex (a) and real (b) impedance harvesting loads.

intrinsic physical properties of the harvester, which, as shown in Fig. 9, can be studied considering the equivalent mechanical effects [48] produced by the coil impedance $Z_e = R_e + j\omega L_e$ and by the harvesting complex impedance load $Z_{h,opt}$, where, according to Eqs. (29) and (58), $Z_{h,opt} = Z^*_{ei} = R_e + \frac{\psi^2_{cm}}{c_m} - j\omega L_e$. As shown in sketch a, the electrical effects of the coil and harvesting complex load produce three equivalent mechanical damping effects in series associated respectively to the resistance of the coil, ψ^2_{cm}/R_e, and to the resistance of the harvesting load, ψ^2_{cm}/R_e and c_m, which have been enbossed in a dashed rectangle to indicate they are generated by the harvesting load. According to the scaling laws presented in Fig. 5a, as depicted in the centre sketch of Fig. 9a, the two damping coefficients ψ^2_{cm}/R_e scale proportionally to $[L^3]$, whereas the damping

coefficient c_m scales proportionally to $[L^1]$ (small scales) and $[L^1]$, $[L^{2.5}]$ (large scales without and with eddy currents damping). Therefore, for small scale harvesters, the damping coefficient c_m becomes sensibly much larger than the damping coefficients ψ_{cm}^2/R_e. As a result the damper c_m acts as a solid element such that, as shown in the lumped parameter model for small scale harvesters, only the dampers due to the resistive effect of the coil, ψ_{cm}^2/R_e, and to resistive effect of the harvesting load, ψ_{cm}^2/R_e, are in fact effective. For small scales, these two elements are characterised by very small damping coefficients so that little energy can be harvested, even for the relatively large strokes that occur for $\omega = \omega_n$. Moving to the large scale harvesters, the phenomenon is reversed. In fact, the damping coefficients ψ_{cm}^2/R_e become sensibly much larger than the damping coefficient c_m, particularly when there are no eddy currents damping effects. Therefore, now, the two dampers ψ_{cm}^2/R_e act as solid elements such that, as shown in the lumped parameter model for the large scale harvesters, only the damper due to the resistive effect of the harvesting load, c_m is effective. This equivalent damping effect is actually equal to the intrinsic mechanical damping of the harvester. Therefore, recalling the maximum power transfer theorem for electric networks [63], it can be noticed that this is indeed the configuration to have maximum power transfer from the source, i.e. the transducer, to the harvesting load, i.e. the equivalent damper c_m. This condition is charactrised by an equal power dissipation by the transducer mechanical damping and the harvesting equivalent damping effect. Therefore, for large scale electromagnetic harvesters, the efficiency is bounded to 50%. This is an intrinsic property of seismic harvesters.

Considering now the case where the optimal real harvesting load $Z_{hR,opt}$ is implemented, as anticipated in Section 3.1, since for the scaling range considered in this study the transducer natural frequency is much lower than the electrical cut-off frequency where the coil inductive effect becomes relevant, i.e. $\omega_n \ll \omega_{ce}$, the expression for the efficiency given in Eq. (75) reduces to the same expression found for the complex harvesting load in Eq. (74), i.e. $E_R \cong E \cong \frac{1}{2}\frac{\Pi_{cm}^2}{2-\Pi_{cm}^2}$. Therefore, also in this case the efficiency depends on the electromagnetic power transduction factor Π_{cm}^2 such that, for small dimensions of the transducer, only a small amount of the input power can be converted into harvested power whereas, for large dimensions of the transducer, a maximum of 50% of the input power can be converted into harvested power. Also in this case the "S-type" scaling law depends on the physical properties of the harvester, which, as shown in Fig. 9b, can be examined considering the equivalent mechanical effects [48] produced by the coil impedance $Z_e = R_e + j\omega L_e$ and by the optimal complex impedance load $Z_{hR,opt}$, where, according to Eqs. (29) and (58), $Z_{hR,opt} = |Z_{ei}| = \sqrt{\left(R_e + \frac{\psi_{cm}^2}{c_m}\right)^2 + (\omega_n L_e)^2}$. In this case, as shown in sketch b, these electrical effects produce an equivalent stiffness and two equivalent damping effects connected in series, which are associated respectively to the inductance and resistance of the coil, ψ_{cm}^2/L_e and ψ_{cm}^2/R_e, and to the resistance of the harvesting load, $\frac{\psi_{cm}^2}{\sqrt{\left(R_e+\frac{\psi_{cm}^2}{c_m}\right)^2+(\omega_n L_e)^2}}$. Again, considering the scaling laws shown in Fig. 5a, as depicted in the centre sketch of Fig. 9b, the stiffness ψ_{cm}^2/L_e and damping ψ_{cm}^2/R_e coefficients scale proportionally to $[L^1]$ and $[L^3]$ respectively. Taking into consideration that the transduction is defined with respect to velocity, and recalling that $\omega = \omega_n$, the effect of the spring results $\psi_{cm}^2/(\omega_n L_e)$, which scales proportionally to $[L^2]$. The spring produces a rather large elastic force in the whole scale range so that it can be considered as a solid element and thus it can be neglected in the lumped parameter model. The scaling of the damping term $\frac{\psi_{cm}^2}{\sqrt{\left(R_e+\frac{\psi_{cm}^2}{c_m}\right)^2+(\omega_n L_e)^2}}$ is somewhat more complex. Nevertheless, considering the scaling laws reported in the sketch, for small scales it can be approximated in terms of a damping coefficient $\frac{\psi_{cm}^2}{R_e}$, which scales proportionally to $[L^3]$. Alternatively, for large scales it can be approximated in terms of the damping coefficient c_m, which scales proportionally to $[L^{2.5}]$, $[L^1]$ depending whether the transducer is or is not affected by eddy currents damping. Therefore, as shown in the lumped parameter model, small scale harvesters are characterised by the coil equivalent damping, $\frac{\psi_{cm}^2}{R_e}$, and the harvesting load equivalent damping $\frac{\psi_{cm}^2}{R_e}$. Both terms are very small and thus little energy can be harvested so that the efficiency tends to 0. In contrast, large scale harvesters are affected only by the harvesting load equivalent damping effect c_m. Therefore, as seen for the optimal complex load, this configuration leads to the maximum energy harvesting possible, which according to the maximum power transfer theorem for electric networks [63], is actually 50% of the input power, so that the efficiency tends to 0.5.

4. Piezoelectric harvester: scaling study

The scaling laws for the physical and energy harvesting properties of the piezoelectric seismic harvester are now addressed. As done for the electromagnetic harvester, first, the characteristic energy expressions are derived considering the harvester is connected to the optimal complex and purely real harvesting loads. Then, the scaling laws of the principal mechanical and electrical physical properties that characterise the harvester are revised. Finally, the scaling of the harvested power and the scaling of the power efficiency are investigated assuming the harvester is excited at its fundamental natural frequency, i.e. ω_n, such that, as shown in Appendix B.2, the maximum power is harvested.

4.1. Energy formulation

Considering first the harvested power, according to the sign convention used in the lumped parameter model shown in Fig. 1d, the following relation holds for the current i_h at the terminals of the harvesting electrical load with admittance Y_h:

$$i_h = -e_h Y_h. \tag{76}$$

Substituting this equation into the matrix expression in Eq. (25), the following relation is derived:

$$e_h = \frac{-T_{iw}}{Y_{ei} + Y_h} \dot{w}_h. \tag{77}$$

Thus the time averaged power harvested with a generic load results:

$$\overline{P}_h = \lim_{T\to\infty} \frac{1}{T} \int_0^T P_h(t) \mathrm{d}t = \frac{1}{2} \mathrm{Re}\{Y_h\} |e_h|^2 = \frac{1}{2} \mathrm{Re}\{Y_h\} \left| \frac{-T_{iw}}{Y_{ei} + Y_h} \right|^2 |\dot{w}_h|^2. \tag{78}$$

Also in this case, using Fermat's theorem [63], the complex electric load Y_h, which maximizes the harvested power at each frequency results given by Ref. [33]:

$$Y_{h,opt} = Y_{ei}^*, \tag{79}$$

where * denotes the complex conjugate. Alternatively, if Y_h is assumed purely real, the optimal electric load results given by Ref. [33]:

$$Y_{hR,opt} = |Y_{ei}|. \tag{80}$$

Substituting Eqs. (79), (80) into Eq. (78), the following expressions are derived for the maximum power harvested for the complex and real optimal loads respectively:

$$\overline{P}_h = \frac{1}{8} \frac{|T_{iw}|^2}{\mathrm{Re}\{Y_{ei}\}} |\dot{w}_h|^2, \tag{81}$$

$$\overline{P}_{hR} = \frac{1}{4} \frac{|T_{iw}|^2}{|Y_{ei}| + \mathrm{Re}\{Y_{ei}\}} |\dot{w}_h|^2. \tag{82}$$

As will be shown in the following section, the sky-hook air damping effect can be neglected for most of the scaling range considered in this study. Thus, setting $c_{am} = 0$ and $\omega = \omega_n$ in Eqs. (81), (82), the maximum power harvested with the complex and real optimal loads results:

$$\overline{P}_h = \frac{1}{8} \frac{k_m m_m}{c_m} \Pi_{pe}^2 |\dot{w}_h|^2, \tag{83}$$

$$\overline{P}_{hR} = \frac{1}{8} \frac{k_m m_m}{c_m} \frac{\Pi_{pe}^2}{\alpha_{pe}} |\dot{w}_h|^2, \tag{84}$$

where Π_{pe}^2 is the power transduction factor defined in Eq. (53). Also, the α_{pe} factor in Eq. (84) is given by:

$$\alpha_{pe} = \frac{1 + \sqrt{1 + \beta_{pe}^2}}{2}, \tag{85}$$

where $\beta_{pe} = \frac{\omega_n}{\omega_{ce}} (1 - \Pi_{pe}^2)$. Here, $\omega_n = \sqrt{k_m/m_m}$ is the transducer fundamental natural frequency whereas $\omega_{ce} = \frac{G_e}{C_e^S} = \frac{\sigma_{pe}}{\epsilon_{33}^S}$ is the electrical cut-off frequency where the electric response of the piezoelectric material switches from resistive to capacitive types.

Moving now to the input power, substituting in Eq. (25) the expression for the voltage e_h derived in Eq. (77), the following mechanical base impedance of the transducer can be derived:

$$Z_{mh} = Z_{me} - \frac{T_{fe}T_{iw}}{Y_{ei} + Y_h}. \tag{86}$$

Therefore, for harmonic vibrations, the time-averaged mechanical input power results given by:

$$\overline{P}_i = \frac{1}{2}\mathrm{Re}\{Z_{mh}\}|\dot{w}_h|^2 = \frac{1}{2}\mathrm{Re}\left\{Z_{me} - \frac{T_{fe}T_{iw}}{Y_{ei} + Y_h}\right\}|\dot{w}_h|^2. \tag{87}$$

Substituting Eqs. (79), (80) in this equation, the input power for the complex and real optimal loads result:

$$\overline{P}_i = \frac{1}{2}\mathrm{Re}\left\{Z_{me} - \frac{T_{fe}T_{iw}}{2\mathrm{Re}\{Y_{ei}\}}\right\}|\dot{w}_h|^2, \tag{88}$$

$$\overline{P}_{iR} = \frac{1}{2}\mathrm{Re}\left\{Z_{me} - \frac{T_{fe}T_{iw}}{Y_{ei} + |Y_h|}\right\}|\dot{w}_h|^2. \tag{89}$$

Considering $c_{am} = 0$ and $\omega = \omega_n$, the two equations above reduce to the following expressions respectively for the optimal complex $Y_{h,opt}$ and purely real $Y_{hR,opt}$ harvester loads:

$$\overline{P}_i = \frac{1}{4}\frac{k_m m_m}{c_m}\left(2 - \Pi_{pe}^2\right)|\dot{w}_h|^2, \tag{90}$$

$$\overline{P}_{iR} = \frac{1}{4}\frac{k_m m_m}{c_m}\left(2 - \frac{4\alpha_{pe}}{4\alpha_{pe}^2 + \beta_{pe}^2}\Pi_{pe}^2\right)|\dot{w}_h|^2. \tag{91}$$

The power efficiency $E = \overline{P}_h/\overline{P}_i$ can now be specified for the piezoelectric energy harvester using Eq. (78) and Eq. (87):

$$E = \frac{\mathrm{Re}\{Y_h\}\left|\frac{T_{iw}}{Y_{ei}+Y_h}\right|^2}{\mathrm{Re}\left\{Z_{me} - \frac{T_{fe}T_{iw}}{Y_{ei}+Y_h}\right\}}. \tag{92}$$

Thus, considering the optimal complex and real admittances $Y_{h,opt} = Y_{ei}^*$ and $Y_{hR,opt} = |Y_{ei}|$ derived in Eqs. (79), (80), the above expression results:

$$E = \frac{1}{4}\,\frac{|T_{iw}|^2}{\mathrm{Re}\{Y_{ei}\}\;\mathrm{Re}\left\{Z_{me} - \frac{T_{fe}T_{iw}}{2\mathrm{Re}\{Y_{ei}\}}\right\}}, \tag{93}$$

$$E_R = \frac{1}{2}\,\frac{|T_{iw}|^2}{(|Y_{ei}| + \mathrm{Re}\{Y_{ei}\})\;\mathrm{Re}\left\{Z_{me} - \frac{T_{fe}T_{iw}}{Y_{ei}+|Y_h|}\right\}}, \tag{94}$$

which, assuming $c_{am} = 0$ and $\omega = \omega_n$, become

$$E = \frac{1}{2}\frac{\Pi_{pe}^2}{2 - \Pi_{pe}^2}, \tag{95}$$

$$E_R = \frac{1}{2}\frac{\Pi_{pe}^2\left(4\alpha_{pe}^2 + \beta_{pe}^2\right)}{2\alpha_{pe}\left(4\alpha_{pe}^2 + \beta_{pe}^2 - 2\alpha_{pe}\Pi_{pe}^2\right)}, \tag{96}$$

respectively for optimal complex and purely real harvesting loads.

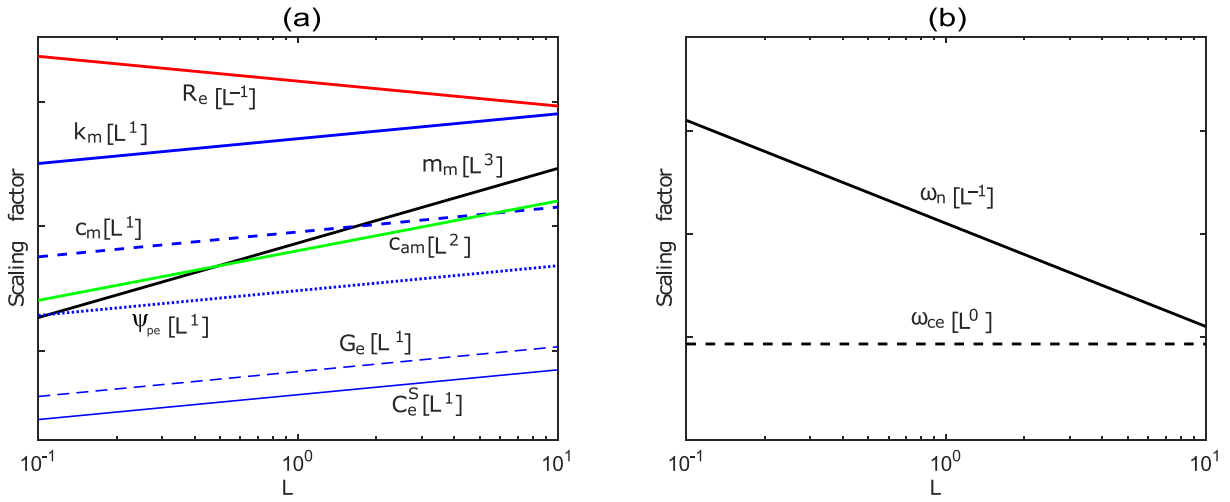

Fig. 10. Scaling laws of (a) moving mass m_m (black solid line), stiffness k_m (blue solid line), air damping coefficient c_{am} (green solid line) and material damping c_m (blue dashed line), transduction coefficient ψ_{pe} (blue dotted line), capacitance C_e^S (blue thin solid line), dielectric conductance G_e (blue thin dashed line), dielectric resistance R_e (red solid line), (b) mechanical natural frequency ω_n (solid line), electrical cut off frequency ω_{ce} (dashed line). (For interpretation of the references to colour in this figure legend, the reader is referred to the Web version of this article.)

4.2. Scaling laws of the characteristic physical parameters

The scaling laws of the lumped parameter elements that compose the piezoelectric transducer shown in Fig. 1c are now revised. Also in this case, the scaling laws can be readily derived recalling that the physical properties of the transducer (e.g. density, Young's modulus of elasticity for the substrate and piezoelectric layers, permittivity, electrical conductivity, strain/charge transduction constant for the piezoelectric layers) do not vary with scale. For instance, according to Eq. (14) the seismic mass of the piezoelectric transducer m_m scales with the cube of dimension, i.e. $[L^3]$. Also, recalling Eq. (15), the natural frequency for the fundamental bending mode of the clamped composite beam and tip mass scales with the inverse of dimension, i.e. $[L^{-1}]$. Therefore the modal stiffness k_m given in Eq. (16) scales proportionally to the dimension, that is $[L^1]$. Considering Eq. (17), the strain-rate damping coefficient is proportional to the material loss factor η_m and modal stiffness k_m and inversely proportional to the fundamental natural frequency. Brantley et al. [64], showed that the material loss factor η_m for the fundamental vibration natural mode of clamped beams scales with the inverse of dimension, i.e. $[L^{-1}]$. Therefore, the equivalent viscous damping coefficient for strain-rate damping scales proportionally to $[L^1]$. The damping ratio $\xi_m = \frac{c_m}{2\sqrt{k_m m_m}} = \frac{\eta_m}{2}$ will thus scale proportionally to the inverse of dimension, i.e. $[L^{-1}]$. For the scale range considered in this study, the damping effect generated by the air loading on the beam is given by Eq. (18). Therefore, the air damping factor c_{am} scales with the second power of dimension, i.e. $[L^2]$. Considering the expression for the piezoelectric transduction coefficient given in Eq.

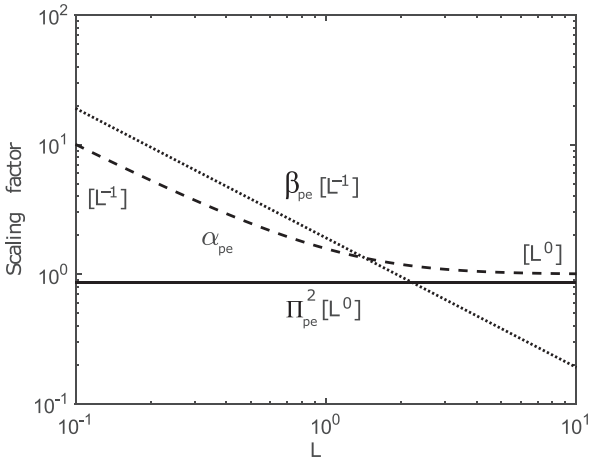

Fig. 11. Scaling laws of piezoelectric power transduction factor Π_{pe}^2 (solid line), capacitance effect coefficient α_{pe} (dashed line), β_{pe} coefficient (dotted line).

(23), it can be readily concluded that ψ_{pe} scales proportionally to dimension, i.e. $[L^1]$. As discussed in Section 2.1, the lossy capacitance of the piezoelectric harvester under constant strain is given by Eq. (20), which indicates that it scales proportionally to dimension, i.e. $[L^1]$. The dissipative effect is actually expressed in terms of the conductance of the piezoelectric layers, which, according to the formulation presented in Section 2.1, is given by $G_e = 2\sigma_{pe}\frac{bL}{h_{pe}}$ and thus scales proportionally to dimension, i.e. with $[\mathrm{L}^1]$.

In summary, as shown in Plot a of Fig. 10, as the size of the transducer is scaled up, the dielectric conductance of the piezoelectric material G_e, the modal stiffness k_m, the mechanical strain-rate damping c_m, the piezoelectric transduction coefficient ψ_{pe} and the constant strain capacitance C_e^S rise proportionally to $[\mathrm{L}^1]$. Also, the air damping c_{am} rises with the power of $[\mathrm{L}^2]$, whereas the modal mass m_m scales proportionally to the cube of dimension, i.e. $[\mathrm{L}^3]$. Finally, the resistance $R_e = 1/G_e$ is bound to scale proportionally to $[\mathrm{L}^{-1}]$. Therefore, as shown in Plot b of Fig. 10, the fundamental natural frequency of the transducer, $\omega_n = \sqrt{k_m/m_m}$, scales with $[L^{-1}]$, whereas the electrical cut-off frequency $\omega_{ce} = G_e/C_e^S$ does not change with dimension, i.e. scale with $[\mathrm{L}^0]$. According to this Plot, when the transducer is about 30 times larger than the reference transducer considered in this study, which has characteristic dimension of 4 cm, the fundamental natural frequency eventually becomes smaller than the electrical cut-off frequency.

The power expressions derived in Section 4.1 are based on the so called piezoelectric power transduction factor Π_{pe}^2, which, as shown in Section 2.3.2, gives the ratio of the power transfer within the transducer per input power to the transducer. Considering Eq. (53), this factor depends on: a) the square of the transduction coefficient $\psi_{pe}^2 = (\mathrm{e}_{31}bz)^2$, b) the damping factor c_m and c) the conductance of the piezoelectric layers G_e. All these parameters scale proportionally to $[\mathrm{L}^1]$. Thus, as shown in Fig. 11, the piezoelectric coupling factor Π_{pe}^2 does not change with the dimension of the transducer, that is, it scales proportionally to $[\mathrm{L}^0]$. The energy harvesting with a real harvesting impedance load also depends on the $\alpha_{pe} = \frac{1+\sqrt{1+\beta_{pe}^2}}{2}$ and $\beta_{pe} = \frac{\omega_n}{\omega_{ce}}(1-\Pi_{pe}^2)$ factors defined in Eq. (85), which, as discussed above, take into account the conductance effect of the piezoelectric material. As can be noticed in Fig. 10b, the cut-off frequency where the electric impedance switches from resistive to capacitive is substantially much smaller than the mechanical fundamental natural frequency, that is $\omega_{ce} \ll \omega_n$, up to about the $4cm$ reference dimension of the transducer considered in this study. For larger dimensions the two characteristic frequencies become progressively similar and, eventually, for scales slightly larger than the range considered here, would even switch such that $\omega_{ce} \gg \omega_n$. This implies that for scales up to about the $4cm$ reference dimension, the transducer is characterised by a capacitive electric response, whereas, for larger scales it is characterised by a resistive and capacitive response. As a result, for scales up to about $4cm$, the coefficient β_{pe} scales proportionally to $[\mathrm{L}^{-1}]$ whereas the α_{pe} factor scales proportionally to $[\mathrm{L}^{-1}]$. Alternatively for larger scales than $4cm$, the α_{pe}factor remains constant, that is scales proportionally to $[\mathrm{L}^0]$. Therefore, considering the power and efficiency expressions derived in Section 4.1, for harvesters having about the same or greater dimension than the $4cm$ reference dimension, the harvested and input powers and the efficiency produced with the optimal real and complex harvesting loads are about the same, i.e.: a) $\overline{P}_{hR} \cong \overline{P}_h \cong \frac{1}{8}\frac{k_m m_m}{c_m}\Pi_{pe}^2|\dot{w}_h|^2$, b) $\overline{P}_{iR} \cong \overline{P}_i \cong \frac{1}{4}\frac{k_m m_m}{c_m}(2-\Pi_{pe}^2)|\dot{w}_h|^2$, c) $E_R \cong E \cong \frac{1}{2}\frac{\Pi_{pe}^2}{2-\Pi_{pe}^2}$. For harvesters with smaller size than the $4cm$ reference dimension, the electric impedance of the

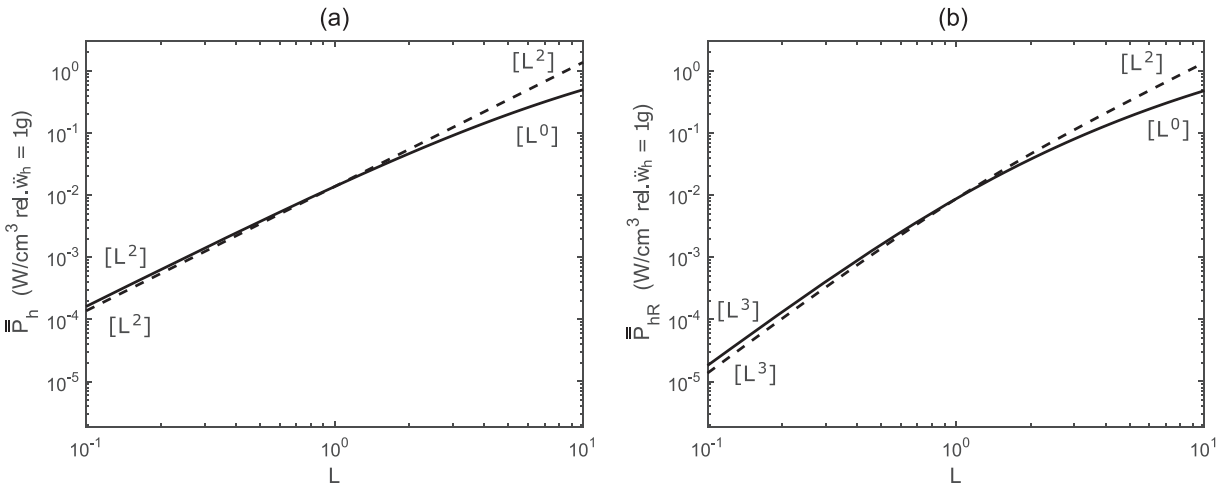

Fig. 12. Scaling laws of the normalised harvested power density $\overline{\overline{P_h}}$ when (a) the optimal complex and (b) optimal purely real electrical loads are implemented and the piezoelectric transducer is (solid line) or is not (dashed line) affected by eddy currents damping.

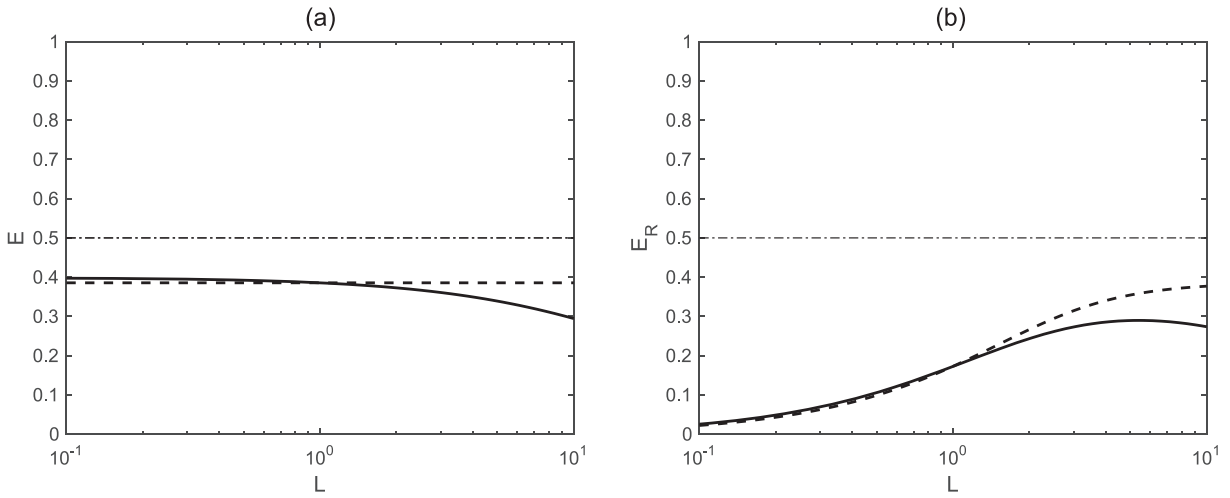

Fig. 13. Scaling laws of the power harvesting efficiency when (a) the optimal complex and (b) optimal purely real electrical loads are implemented and the piezoelectric transducer is (solid line) or is not (dashed line) affected by air damping.

transducer would show a capacitive impedance, which cannot be compensated by the purely real harvesting load. As a result, part of the input power would be stored in the piezoelectric capacitive layers and not transmitted to the harvesting load. From the mathematical point of view, this reflects into an α_{pe} factor that scales proportionally to $[L^{-1}]$ such that the harvested and input power and the harvesting efficiency produced by the optimal real harvesting load are smaller than those generated with the complex harvesting load.

4.3. Scaling laws of the normalised power density and efficiency

The scaling laws for the normalised harvested power density and for the power harvesting efficiency of the piezoelectric harvester are now analysed. As seen for the electromagnetic harvester, the normalised harvested power density $\overline{\overline{P_h}} = \frac{\overline{P}_h}{V_h}\Big|_{\ddot{w}_h=1g}$ is given by the time-averaged harvested power $\overline{P}_h$ per unit volume of the transducer V_h, assuming $1g$ base acceleration at $\omega = \omega_n$. As done for the electromagnetic harvester, the scaling laws were derived numerically from Eqs. (83), (84) and (95), (96), considering the scaling of the lumped elements shown in Figs. 10 and 11.

Fig. 12 shows the scaling laws of the normalised power density for both complex and purely real optimal electric loads when the contribution of the air damping is neglected (dashed line) and when is taken into account (solid line). Plots a and b indicate that for both optimal harvesting loads the normalised power density monotonically rises as the size of the device is increased. More precisely, considering the case with optimal complex harvesting load, the scaling of the harvested power density is characterised by two asymptotes with respect to the $4cm$ reference harvester considered in this study: for small dimensions, it scales proportionally to $[L^2]$, whereas, for large dimensions, it scales proportionally to $[L^0]$. Alternatively, considering the case with optimal real harvesting load, for small dimensions, it scales proportionally to $[L^3]$, whereas, for large dimension, it scales proportionally to $[L^0]$. If the harvesters were operated in vacuum such that no air damping acted on the cantilever beam, as shown by the dashed lines, the scaling laws would vary particularly at the higher end of the scaling range. Indeed, considering the case with optimal complex harvesting load, the scaling of the harvested power density would be proportional to $[L^2]$ in the whole range considered. Alternatively, for the case with optimal real harvesting load, the scaling would be proportional to $[L^3]$ for small dimension and proportional to $[L^2]$ for large dimensions. In general, contrasting the two diagrams, it can be noticed that, for small scales, the optimal complex harvesting load absorbs more power than the optimal real load. In contrast, for large scales, the two harvesting loads produce about the same levels of harvested power.

Moving to power efficiency, Plot a in Fig. 13 shows that, when the optimal complex impedance load given in Eq. (79) is implemented, the piezoelectric seismic harvester is characterised by a somewhat constant efficiency of 0.4, which eventually drops proportionally to $[L^{-1}]$ for very large scales. If the air damping effect is neglected, the efficiency becomes constant and equal to 0.4 in the whole scaling range considered in this study. Moving to Plot b, when the optimal purely real electric load derived in Eq. (80) is implemented, the efficiency of the device is characterised by an "S-type" law. Thus it increases with dimension and, in case of solely material damping contribution, according to the dashed line, it converges to the same constant value obtained in Plot a for the complex impedance load when the effect of the air damping is not taken into account. If the contribution of the air damping is also considered, the solid line indicates that the efficiency has a maximum value for a scale about 5 times greater than the $4cm$ reference dimension and then falls down at larger scales.

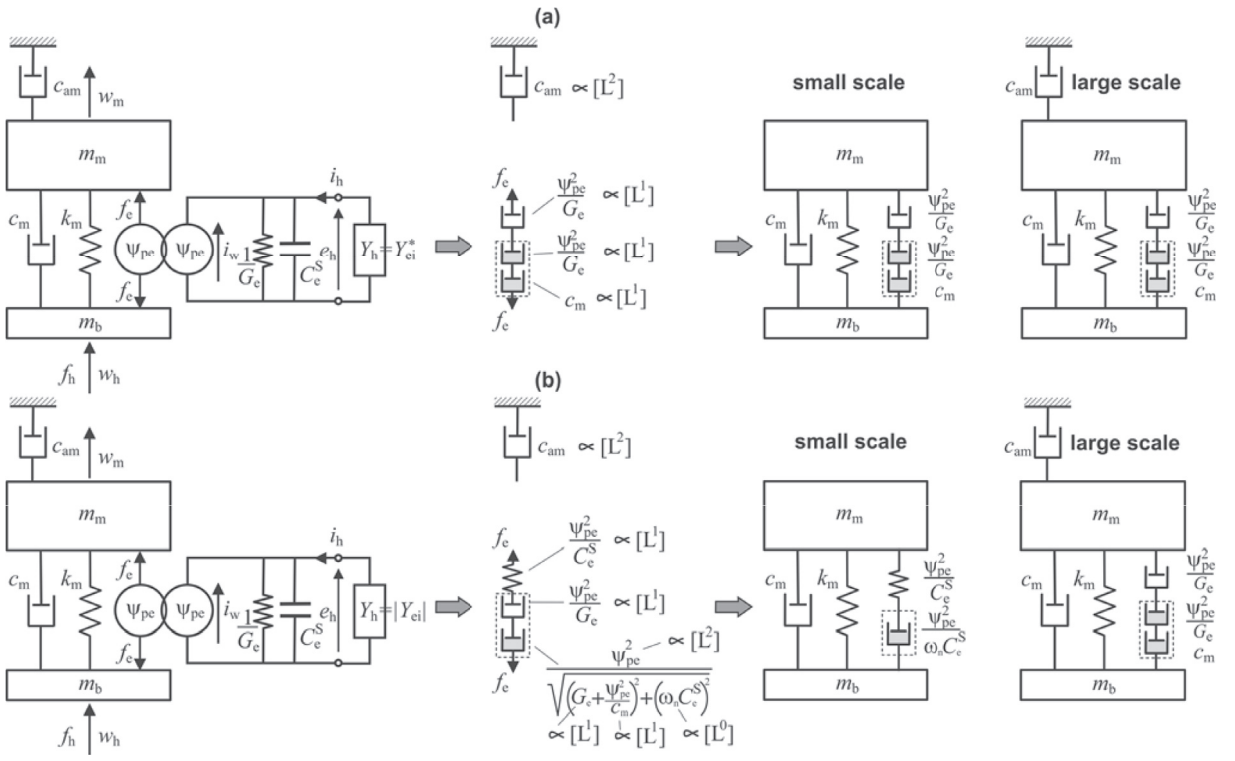

Fig. 14. Sketches of the equivalent mechanical effects produced by the electrical components of small scale and large scale piezoelectric harvesters with optimal complex (a) and real (b) impedance harvesting loads.

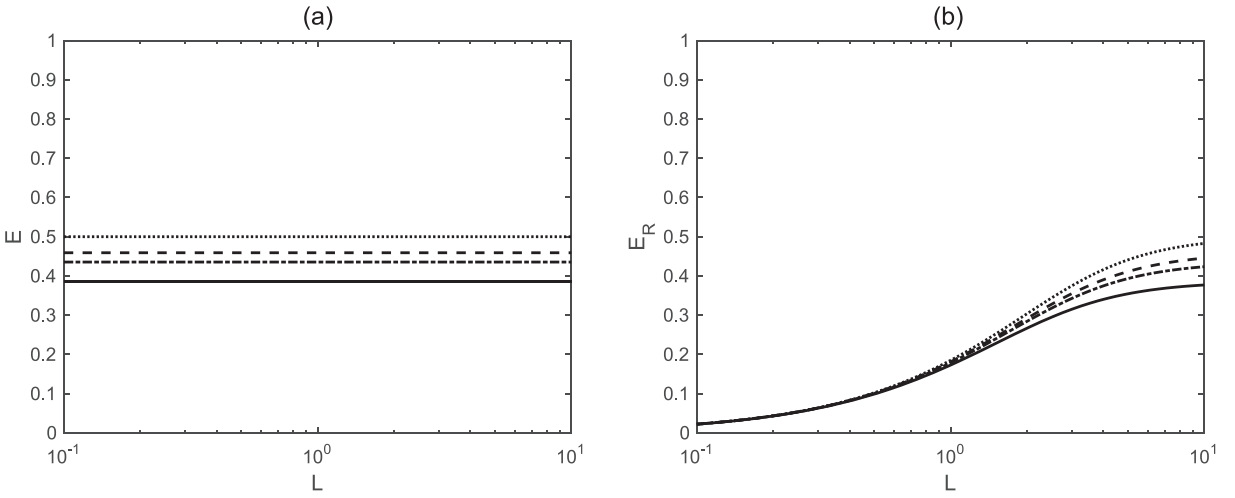

Fig. 15. Scaling laws of the power harvesting efficiency when (a) the optimal complex and (b) optimal purely real electrical loads are implemented assuming the piezoelectric transducer is not affected by air damping and, assuming $\sigma_{pe} = 4.5 \cdot 10^{-8}\ S/m$, the conductivity of the piezoelectric layers is equal to $1\sigma_{pe}$ (solid line), $0.5\sigma_{pe}$ (dash dotted line), $0.3\sigma_{pe}$ (dashed line), $0\sigma_{pe}$ (dotted line).

Considering first the case where the optimal complex harvesting load $Z_{h,opt}$ is implemented, according to Eq. (95), the energy harvesting efficiency solely depends on the piezoelectric power transduction factor Π^2_{pe}. In-depth analysis of Eq. (95) and of the scaling plot for Π^2_{pe} shown in Fig. 11 confirms that the efficiency is bound to a constant value, whose amplitude depends on the physical properties of the harvester. As done for the electromagnetic harvester, the intrinsic physics of the harvester can be unfolded by considering the equivalent mechanical effects produced by the admittance of the piezoelectric

layers $Y_e = \frac{1}{Z_e} = \mathrm{j}\omega\tilde{C}_e^S = \mathrm{j}\omega C_e^s + G_e$ and the admittance of the optimal complex load, which, according to Eqs. (79) and (38) is given by $Y_{h,opt} = Y_{ei}^* = -\mathrm{j}\omega C_e^s + G_e + \frac{\psi_{pe}^2}{c_m}$. Here, $C_e^S = 2\varepsilon_{33}^S \frac{bL}{h_{pe}}(1 - k_{31}^2)$, $G_e = 2\sigma_{pe}\frac{bL}{h_{pe}}$ and $\psi_{pe} = e_{31}bz$. As shown in sketch a of Fig. 14, the electrical effects of the piezoelectric layers and harvesting complex load produce three equivalent mechanical damping effects in series, ψ_{pe}^2/G_e, ψ_{pe}^2/G_e, c_m, associated respectively to the resistance of the piezoelectric layer $1/G_e$ and to the resistances of the harvesting load $1/G_e$ and c_m, which have been embossed in a dashed rectangle to indicate they are generated by the harvesting load. According to the scaling laws presented in Fig. 10a, as depicted in the centre sketch of Fig. 14a, all three elements scale proportionally to $[L^1]$. Therefore, they all play a role in the energy harvesting, which can be conveniently identified by considering first the case in which the piezoelectric layers were not affected by dielectric losses such that $\psi_{pe}^2/G_e \to \infty$. In this case the electric effects of the piezoelectric layers and harvesting complex load would reduce to a mere damping term c_m, so that, according to maximum power transfer theorem for electric networks, the maximum power harvesting would be produced, which is actually 50% of the input power since the other 50% would be absorbed by the mechanical damping c_m of the transducer. Therefore, in case the piezoelectric layers were not affected by dielectric losses, the efficiency would be bounded to maximum level of 0.5 for all scales. In practice, the harvester is also characterised by a sky-hook mechanical damping due to the air load acting on the harvesting beam c_{am}, which, as shown in the sketch a, scales proportionally to $[L^2]$ and thus becomes relevant for large scales. In this case, as can be observed in plot a of Fig. 13, the harvesting efficiency remains constant up to about the $4cm$ reference dimension considered in this study and then monotonically drops proportionally to $[L^{-1}]$. Now, if the piezoelectric layers are also affected by dielectric losses, then there would be an extra loss of power in the layers themselves, which is proportional to ψ_{pe}^2/G_e. Therefore, the efficiency would still remain constant for small scales, but would be smaller than 0.5. Fig. 15a shows exactly how, in absence of air damping, the constant efficiency level would shift down from the limiting value of 0.5 to about 0.38 as the electric conductivity σ_{pe} of the dielectric material in the piezoelectric layers rises from 0 to $4.5 \cdot 10^{-8} S/m$.

As anticipated in Section 4.2, for scales equal to or larger than the $4cm$ reference dimension considered in this study, the power harvesting efficiency with the real optimal load is actually about the same as that for the optimal complex harvesting load and thus depends only on the piezoelectric coupling factor Π_{pe}^2. Alternatively, for small scales up to the 4 cm reference dimension, it also depends on the α_{pe} and β_{pe} factors defined in Eq. (85), which include the conductance effect of the piezoelectric material. As shown in Plot b of Fig. 13, this give rise to quite a different efficiency scaling law than that shown in Plot a for the complex harvesting load. Once again this results from the intrinsic physics of the harvester, which can be analysed considering the equivalent mechanical effects produced by the admittance of the piezoelectric layers $Y_e = \frac{1}{Z_e} = \mathrm{j}\omega\tilde{C}_e^S = \mathrm{j}\omega C_e^s + G_e$ and the admittance of the optimal complex load, which, according to Eqs. (80) and (43) is given by $Y_{hR,opt} = |Y_{ei}| = \sqrt{(\omega_n C_e^s)^2 + \left(G_e + \frac{\psi_{pe}^2}{c_m}\right)^2}$. In this case, as shown in the centre sketch of Fig. 14b, these electrical effects produce an equivalent stiffness and two equivalent damping effects connected in series, which are associated respectively to the

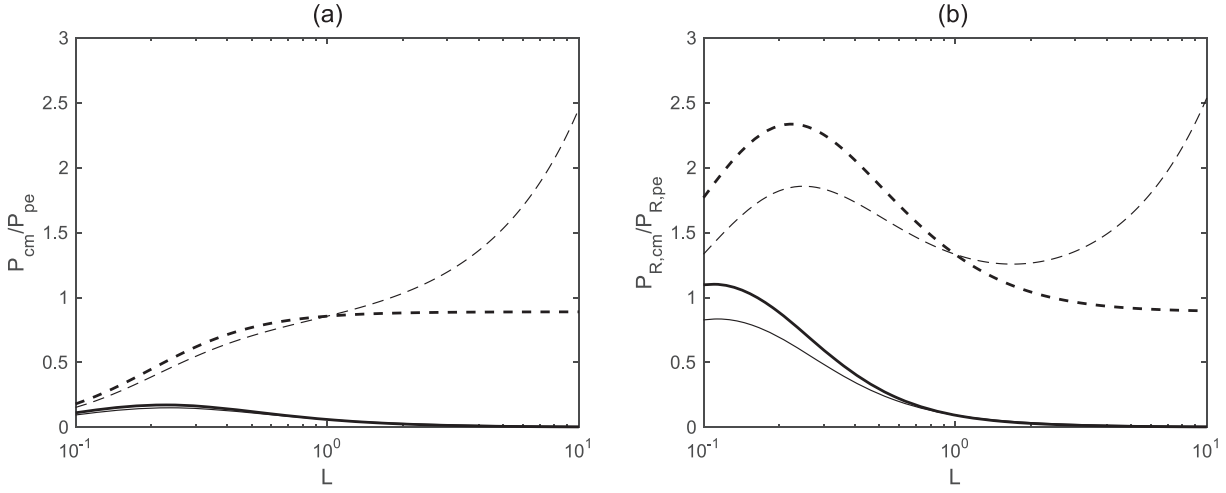

Fig. 16. Electromagnetic and piezoelectric harvesters power harvested ratios for (a) the optimal complex and (b) the real electrical loads considering the following cases: i) thin-solid line, with eddy currents damping and with beam air damping; ii) thick-solid line, with eddy currents damping and without beam air damping; iii) thin-dashed line, without eddy currents damping and with beam air damping; iv) thick-dashed line, without eddy currents damping and without beam air damping.

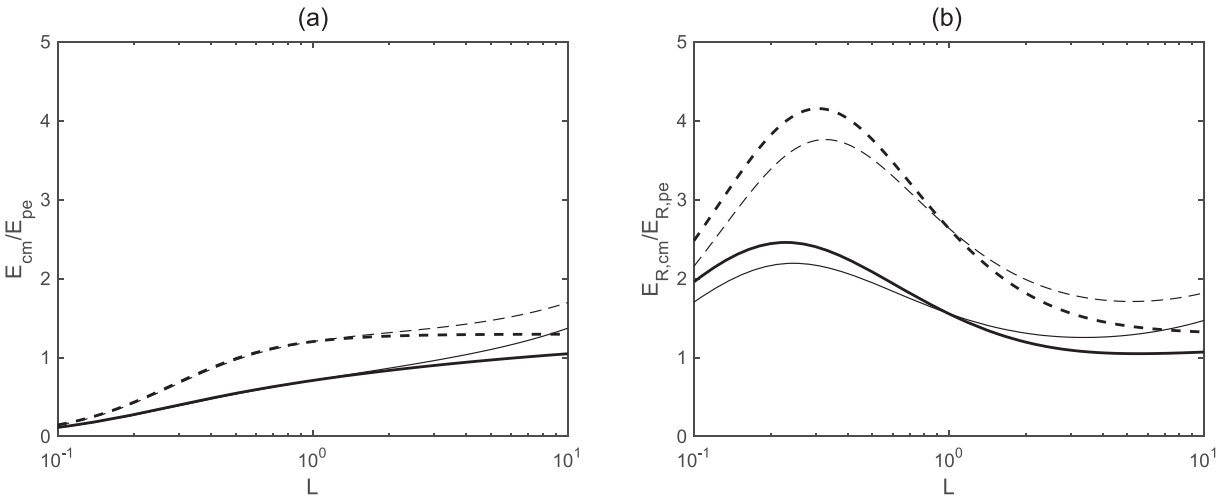

Fig. 17. Electromagnetic and piezoelectric harvesters efficiency ratios for (a) the optimal complex and (b) the real electrical loads considering the following cases: i) thin-solid line, with eddy currents damping and with beam air damping; ii) thick-solid line, with eddy currents damping and without beam air damping; iii) thin-dashed line, without eddy currents damping and with beam air damping; iv) thick-dashed line, without eddy currents damping and without beam air damping.

capacitance and conductance of the piezoelectric layers, ψ_{pe}^2/C_e^s and ψ_{pe}^2/G_e, and to the resistance of the harvesting load, $\frac{\psi_{pe}^2}{\sqrt{(\omega_n C_e^s)^2+\left(G_e+\frac{\psi_{pe}^2}{c_m}\right)^2}}$. Again, considering the scaling laws shown in Fig. 10a, the stiffness ψ_{pe}^2/C_e^s and damping $\psi_{pe}^2/\,G_e$ coefficients scale proportionally to $[L^1]$. Taking into consideration that the transduction is defined with respect to velocity, and recalling that $\omega = \omega_n$, the effect of the spring results $\psi_{pe}^2/(\omega_n C_e^s)$, which scales proportionally to $[L^2]$. The scaling of the damping term $\frac{\psi_{pe}^2}{\sqrt{(\omega_n C_e^s)^2+\left(G_e+\frac{\psi_{pe}^2}{c_m}\right)^2}}$ requires instead a more involved analysis. For instance, considering the scaling laws of the terms in the expression shown in the sketch, for small scales it can be approximated in terms of a damping coefficient $\psi_{pe}^2/\,(\omega_n C_e^s)$, which scales proportionally to $[L^2]$. Alternatively, for large scales it can be approximated in terms of the damping coefficient c_m, which scales proportionally to $[L^1]$. Therefore, as shown in the lumped parameter model, small scale harvesters are characterised by the equivalent stiffness, $\frac{\psi_{pe}^2}{C_e^s}$ and the harvesting load equivalent damping $\frac{\psi_{pe}^2}{\omega_n C_e^s}$, which scale proportionally to $[L^1]$ and $[L^2]$ respectively. Thus, the equivalent damping term produced by the harvesting load scales down at a greater rate than the mechanical damping of the transducer c_m, which instead scales proportionally to $[L^1]$. Therefore, most of the input power is dissipated by the transducer and only a smaller portion by the harvesting load. As a result, the harvesting efficiency is relatively low, as shown in Plot b of Fig. 13. Alternatively, as shown in the lumped parameter model, large scale harvesters are characterised by three dampers in series: the damper $\frac{\psi_{pe}^2}{G_e}$ produced by the dielectric conductance of the piezoelectric layers and the dampers $\frac{\psi_{pe}^2}{G_e}$ and c_m generated by the harvesting load. All three damping effects scale proportionally to $[L^1]$. Therefore in this case the equivalent damping effect produced by the harvesting load scales with the same rate than the intrinsic mechanical damping c_m of the transducer. However, part of the input energy to the transducer is also dissipated by the dielectric conductivity of the piezoelectric layer, which produces an equivalent damping effect $\frac{\psi_{pe}^2}{G_e}$. Therefore, overall, for large scale harvesters the maximum efficiency of 0.5 cannot be reached. Actually, as can be noticed in plot b of Fig. 13, it is further limited by the additional loss produced by the air damping c_{am}, which scales proportionally to $[L^2]$ and thus becomes relevant for large scales producing a peak efficiency value for harvesters about 5 times larger than the $4cm$ reference one. Once more, all these effects are strongly influenced by the dielectric losses. For instance, as shown in Fig. 15b, the peak efficiency would shift down from about 0.5 to about 0.38 as the electric conductivity σ_{pe} of the dielectric material in the piezoelectric layers rises from 0 to $4.5 \cdot 10^{-8} S/m$.

5. Comparative analysis

Comparative scaling studies are now presented for the harvested power and for the power harvesting efficiency with the electromagnetic and piezoelectric seismic transducers. The studies assume the two transducers have the same seismic mass m_m and the same stiffness k_m. Therefore they also have equivalent fundamental natural frequency ω_n.

Figs. 16 and 17 show respectively the ratio of the harvested powers $\frac{\overline{\overline{P}}_{h.cm}}{\overline{\overline{P}}_{h.pe}}$ and the ratio of the power harvesting efficiencies $\frac{E_{cm}}{E_{pe}}$ assuming either the optimal complex (Plots a) or the optimal real (Plots b) electrical loads are implemented. The following four cases are considered for the damping effects in the two transducers: i) with eddy currents damping and with beam air damping (thin-solid line); ii) with eddy currents damping and without beam air damping (thick-solid line) iii) without eddy currents damping and with beam air damping (thin-dashed line); iv) without eddy currents damping and without beam air damping (thick-dashed line).

The ratio of the harvested powers shown in Fig. 16 is first considered. Assuming the optimal complex harvesting load is implemented, the thick-solid and thin-solid lines in Plot a show that, when the electromagnetic harvester is affected by high eddy currents damping, regardless whether or not the piezoelectric beam is affect by air damping, the electromagnetic harvester collects comparatively much less power than the piezoelectric harvester, particularly at the higher end of the scaling range considered in the study. However, the thick-dashed and the thin-dashed lines indicate that, when the electromagnetic harvester is designed in such a way as to avoid eddy currents damping, for larger dimensions than the 4 *cm* reference scale, the electromagnetic harvester collects about the same amount of power than the piezoelectric harvester without air damping (thick-dashed line), or even an increasingly larger amount of power than the piezoelectric harvester with air damping (thin-dashed line). In contrast, for increasingly smaller dimensions of the transducers than the 4 *cm* reference scale, the electromagnetic harvester accumulates progressively less power than the piezoelectric harvester regardless the piezoelectric transducer is or is not affected by air damping. Modelling damping is always a challenging task and thus it is important to specify that the results presented in Fig. 16a are based on the damping factors identified in Ref. [33] for the 4 *cm* reference harvesters considered in this study. Nevertheless, these results provide a realistic qualitative comparison of the power harvested by equal size electromagnetic and piezoelectric harvesters. Thus, in general it can be concluded that, when the harvesters are connected to optimal complex loads, eddy currents greatly limits the power that can be harvested with the electromagnetic transducer. Alternatively, when the electromagnetic harvester is not affected by eddy currents, for small scales than the reference 4 *cm* dimension, it still produces less power than the piezoelectric harvester whereas, for larger scales than the 4*cm* dimension, it produces about the same level of power than the piezoelectric harvester in vacuum such that there is no air damping, and, comparatively more power than the piezoelectric harvester in air such that there is a significant air damping effect.

Considering now the case where the optimal real harvesting loads are implemented, the thick-solid and thin-solid lines in Plot b show that, when the electromagnetic harvester is affected by high eddy currents damping, regardless the piezoelectric beam is or is not affect by air damping, for the smaller end of the scale range considered in this study, the electromagnetic harvester absorbs about the same level of power than the piezoelectric harvester. Alternatively for scales equal or greater that the reference 4*cm* dimension, the electromagnetic harvester absorbs much less power than the piezoelectric harvester. Moving to the case where the electromagnetic harvester is not affected by eddy currents damping, the thick-dashed and the thin-dashed lines indicate that, in general, the electromagnetic harvester outperforms the piezoelectric harvester regardless the latter is or is not affected by air damping. More specifically, when the piezoelectric transducer is not affected by air damping, the electromagnetic harvester results comparatively much more effective for scales about one tenth than the reference 4*cm* dimension. Also, for larger scales than the reference 4*cm* dimension, it tends to produce about the same level of power than the piezoelectric harvester, which actually corresponds to that found for the complex optimal load. Alternatively, when the piezoelectric harvester is affected by air damping, the electromagnetic harvester tends to collect much more power also for large scales. In general, these results indicate that, when the optimal real loads are implemented, apart from the case where the electromagnetic harvester is affected by eddy currents damping, the electromagnetic harvester absorbs comparatively more power than the piezoelectric harvester, particularly when the latter is affected by air damping. There is therefore quite a significant difference when the two harvesters are operated with the optimal complex or optimal real harvesting loads. This is principally due to the fact that, at the fundamental natural frequency of operation ω_n, the electromechanical response of the piezoelectric transducer is strongly affected by a capacitive electric effect of the piezoelectric layers, which tend to store energy and thus prevent the energy transfer to the load. Therefore, the optimal complex load compensates this capacitive effect and thus avoids energy is stored in the transducer rather than transferred to the electric load. The electromagnetic harvester is instead characterised by a resistive effect at the fundamental natural frequency of operation ω_n. Therefore, there is maximum power transfer to the electric load regardless the optimal complex or optimal real loads are implemented.

To conclude this analysis, it is interesting to note that, for the cases where the piezoelectric harvester is not affected by air damping, the harvested power ratio considering the optimal complex and optimal real loads can be simply expressed with the following laws:

$$\frac{\overline{P}_{h,cm}}{\overline{P}_{h,pe}} = \frac{c_{m,pe}}{c_{m,cm}} \frac{\Pi^2_{cm}}{\Pi^2_{pe}}, \tag{97}$$

$$\frac{\overline{P}_{hR,cm}}{\overline{P}_{hR,pe}} = \frac{c_{m,pe}\alpha_{pe}}{c_{m,cm}\alpha_{cm}} \frac{\Pi^2_{cm}}{\Pi^2_{pe}}. \tag{98}$$

The ratio of the harvesting efficiencies shown in Fig. 17 is now considered. Assuming the optimal complex harvesting load is implemented, the thick-solid and thin-solid lines in Plot a show that, when the electromagnetic harvester is affected by high eddy currents damping, regardless whether or not the piezoelectric beam is affect by air damping, the electromagnetic harvester is less efficient in absorbing power than the piezoelectric harvester. The thin line indicates that for large scales than the 4*cm* reference scale, the electromagnetic harvester is actually slightly more efficient than the piezoelectric harvester affected by air damping. Alternatively, the thick-dashed and the thin-dashed lines indicate that, when the electromagnetic harvester is designed in such a way as to avoid eddy currents damping, for larger dimensions than about half the 4*cm* reference scale, the electromagnetic harvester is slightly more efficient than the piezoelectric harvester, regardless the latter is or is not affected by air damping. Actually, when the piezoelectric harvester is affected by damping, for scales greater than three times the 4*cm* reference dimension, the electromagnetic harvester shows a much larger efficiency. Thus, it can be concluded that, for smaller scales compared to the 4*cm* reference dimension, the electromagnetic harvester is generally much less efficient than the piezoelectric transducer. Alternatively, for larger scales compared to the 4*cm* reference dimension, the electromagnetic harvester has about the same or slightly greater efficiency than the piezoelectric harvester. Actually, when the piezoelectric transducer is affected by air damping, the electromagnetic harvester results significantly more efficient than the piezoelectric harvester at the higher end of the considered scaling range.

Considering now the case where the optimal real harvesting loads are implemented, the whole set of curves in Plot b indicate that, the electromagnetic harvester is more efficient than the piezoelectric harvester. More specifically, for smaller scales than the 4*cm* reference diemension, depending whether or not the electromagnetic harvester is affected by high eddy currents damping, it results about two times or four times more efficient than the piezoelectric transducer with or without air damping. Alternatively, for larger scales than the 4*cm* reference dimension, the electromagnetic harvester tends to about the same or to about twice efficiency than the piezoelectric transducer. Also in this case, for larger scales than the 4*cm* reference dimension, the efficiency of the electromagnetic harvester becomes even more larger when the piezoelectric harvester is affected by air damping. As discussed above for the harvested power, these results spring up from the fact that, at the fundamental natural frequency of operation ω_n, the electromechanical response of the piezoelectric transducer is characterised by a capacitive dielectric effect of the piezoelectric layers, which tends to store energy and thus prevents the energy transfer to the load. The real harvesting load cannot compensate this capacitive effect and thus the efficiency of the piezoelectric harvester falls down. This is not the case for the electromagnetic harvester, which is instead characterised by a resistive electrical effect at the fundamental natural frequency of operation ω_n and thus can be effectively set to transfer power to both the complex and real optimal loads.

As seen above, also for the ratio of the efficiencies the harvested power ratio considering the optimal complex and optimal real loads can be simply expressed with the following laws when the piezoelectric harvester is not affected by air damping:

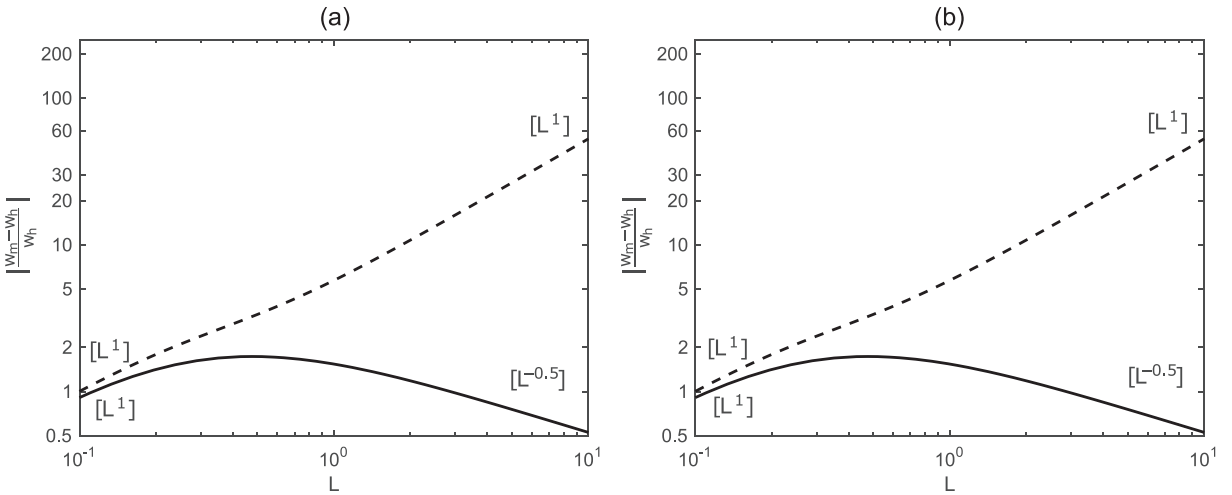

Fig. 18. Scaling laws for the stroke per unit base displacement at $\omega = \omega_n$ of the electromagnetic seismic harvester with (solid line) and without (dashed line) the effect of the eddy currents and connected to (a) the optimal complex and (b) the optimal real harvesting loads.

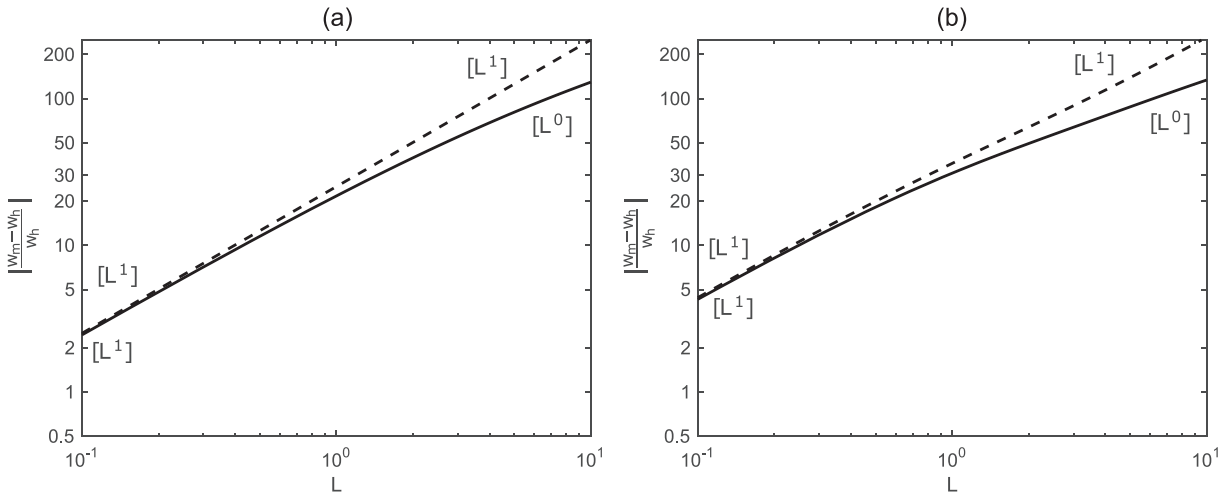

Fig. 19. Scaling laws for the stroke per unit base displacement at $\omega = \omega_n$ of the piezoelectric seismic harvester with (solid line) and without (dashed line) the effect of air damping and connected to (a) the optimal complex and (b) the optimal real harvesting loads.

$$\frac{E_{cm}}{E_{pe}} = \frac{\frac{\Pi_{cm}^2}{2-\Pi_{cm}^2}}{\frac{\Pi_{pe}^2}{2-\Pi_{pe}^2}}. \tag{99}$$

$$\frac{E_{R,cm}}{E_{R,pe}} = \frac{\frac{\Pi_{cm}^2\left(4\alpha_{cm}^2+\beta_{cm}^2\right)}{2\alpha_{cm}\left(4\alpha_{cm}^2+\beta_{cm}^2-2\alpha_{cm}\Pi_{cm}^2\right)}}{\frac{\Pi_{pe}^2\left(4\alpha_{pe}^2+\beta_{pe}^2\right)}{2\alpha_{pe}\left(4\alpha_{pe}^2+\beta_{pe}^2-2\alpha_{pe}\Pi_{pe}^2\right)}}. \tag{100}$$

6. Transducers stroke: scaling study

As discussed for example in Refs. [37,46,65], to properly characterise the response of seismic transducers, the stroke, that is the displacement of the moving mass with respect to the base mass, should also be investigated. Therefore, to fully characterise the energy harvesting with the two systems considered in this study, the scaling laws are now discussed for the strokes of the electromagnetic and piezoelectric seismic transducers excited by a base harmonic displacement at the fundamental natural frequency ω_n. The study assumes that the harvesters can withstand any displacement, although in practice the stroke is normally limited by geometrical constrains (e.g. end stops for the coil magnet harvester) or stiffening effects of the elastic component (e.g. non linear bending deformation of the beam harvester).

Considering first the electromagnetic transducer, inspection of the lumped parameter scheme shown in Fig. 1b leads to the following equation of motion for the seismic mass and Kirchhoff equation for the electric mesh:

$$Z_m(\dot{w}_m - \dot{w}_h) = -Z_s(\dot{w}_m - \dot{w}_h) + \psi_{cm} i_h - Z_m \dot{w}_h, \tag{101}$$

$$e_h = \psi_{cm}(\dot{w}_m - \dot{w}_h) + Z_e i_h. \tag{102}$$

Inspection of the lumped parameter element scheme in Fig. 1d provides two similar equations for the piezoelectric harvester

$$Z_m(\dot{w}_m - \dot{w}_h) = -Z_s(\dot{w}_m - \dot{w}_h) + \psi_{pe} i_h - Z_m \dot{w}_h, \tag{103}$$

$$i_h = \psi_{pe}(\dot{w}_m - \dot{w}_h) + Y_e e_h. \tag{104}$$

Table 1
Scaling properties for the electromagnetic harvester.

Parameter	Symbol − Expression		Case	Small Scale	Ref.ce Scale 4 cm	Large Scale
Suspended comp. mass	m_m			$[L^3]$		$[L^3]$
Springs stiffness	k_m			$[L^1]$		$[L^1]$
Natural frequency	ω_n			$[L^{-1}]$		$[L^{-1}]$
Couette air flow damping	c_a			$[L^1]$		
Eddy currents damping	c_{ec}					$[L^{2.5}]$
Coil resistance	R_e			$[L^{-1}]$		$[L^{-1}]$
Coil inductance	L_e			$[L^1]$		$[L^1]$
Cut-off frequency resistive-inductive	ω_{ce}			$[L^{-2}]$		$[L^{-2}]$
Electromagnetic transduction coefficient	ψ_{cm}			$[L^1]$		$[L^1]$
Electromagnetic power transduction factor	Π^2_{cm}	Eq. (49)		$[L^2]$		$[L^0]$
Harvested power density per 1 g base acceleration	$\overline{P}_h \Big\vert_{\ddot{w}_h=9.81\ m/s^2}$	Eqs. (59,61)	with eddy currents	$[L^4]$		$[L^{0.5}]$
Complex optimal load			without eddy currents	$[L^4]$		$[L^2]$
Harvested power density per 1 g base acceleration	$\overline{P}_{hR} \Big\vert_{\ddot{w}_h=9.81\ m/s^2}$	Eqs. (60,62)	with eddy currents	$[L^4]$		$[L^0]$
Real optimal load			without eddy currents	$[L^4]$		$[L^2]$
Power harvesting efficiency	E	Eqs. (72,74)	with eddy currents	≈ 0	≈ 0.25	≈ 0.5
Complex optimal load			without eddy currents	≈ 0	≈ 0.5	≈ 0.5
Power harvesting efficiency	E_R	Eqs. (73,75)	with eddy currents	≈ 0	≈ 0.25	≈ 0.5
Real optimal load			without eddy currents	≈ 0	≈ 0.5	≈ 0.5
Transducer stroke per unit base displacement	$\frac{w_m - w_h}{w_h}$	Eq. (105)	with eddy currents	$[L^1]$		$[L^{-0.5}]$
Complex & real loads			without eddy currents	$[L^1]$		$[L^1]$

Also, according to the notation shown in Fig. 1b and d, the relations in Eqs. (54) and (76) hold for the impedances and admittances of the harvesting loads respectively. After some mathematical manipulations Eqs. (101), (102) and Eqs. (103), (104) combined respectively with Eq. (54) and Eq. (76) give the following relations for the stroke per unit base displacement of the electromagnetic and piezoelectric harvesters respectively

$$\frac{w_m - w_h}{w_h} = -\frac{Z_m}{Z_t + \frac{\psi_{cm}\psi_{cm}}{Z_e + Z_h}}, \tag{105}$$

$$\frac{w_m - w_h}{w_h} = -\frac{Z_m}{Z_t + \frac{\psi_{pe}\psi_{pe}}{Y_e + Y_h}}. \tag{106}$$

Figs. 18 and 19 show the simulated scaling laws of the stroke per unit base displacement for the two transducers, assuming they are connected to the optimal complex loads (Plots a), given in Eqs. (57), (79), and to the optimal real loads (Plots b), given in Eqs. (58), (80). The simulations are performed assuming that the transducers operate at their fundamental natural frequency $\omega_n = \sqrt{k_m/m_m}$. The graphs for the electromagnetic seismic transducer depicted in Fig. 18 show very similar scaling laws when the optimal complex (Plot a) and purely real (Plot b) harvesting loads are implemented. Considering first the case where the transducer is affected by eddy currents damping, as shown by the solid lines, the stroke amplitude grows proportionally to the first power of dimension i.e. $[L^1]$, reaches a peak value at about half the $4cm$ reference dimension considered in this study, and then, at larger scales, it progressively decreases and falls down with power -0.5 of dimension, i.e $[L^{-0.5}]$. Instead, when the transducer is not affected by eddy currents damping, according to the dashed lines, the stroke is characterised by a monotonically rising law, which for small scales is proportional to $[L^1]$ and for large scales is proportional to $[L^1]$. In general, when the transducer is affected by eddy currents damping, the maximum stroke in the considered scaling range is about twice the amplitude of the base displacement. Instead, when the transducer does not show eddy currents damping, the stroke monotonically rises with scale, such that, for the largest dimension considered in study, the stroke of the transducer is about 50 times the base displacement. This is a very large value, which, indicate, large electromagnetic harvesters can function correctly only with small amplitude ambient vibrations.

Moving to the piezoelectric seismic transducer, the dashed lines in the two plots of Fig. 19 show that, when the transducer is not affected by air damping, the strokes grow monotonically, proportionally to $[L^1]$ both when the complex and real optimal loads are implemented. At the lower scale end, the stroke is about 2 and 5 times the base displacement, whereas at the higher scale end, it is about 200 times the base displacement. The solid lines in the two plots, indicate that when the transducer is affected by air damping the scaling laws rise at a smaller rate that eventually for very large scales levels to $[L^0]$, both when the complex and real optimal loads are implemented. As a result, at the higher scale end, the strokes result about 110 times

Table 2
Scaling properties for the piezoelectric harvester.

Parameter	Symbol − Expression		Case	Small Scale	Ref.ce Scale 4 cm	Large Scale
Suspended comp. mass	m_m			$[L^3]$		$[L^3]$
Beam flexural stiffness	k_m			$[L^1]$		$[L^1]$
Natural frequency	ω_n			$[L^{-1}]$		$[L^{-1}]$
Strain-rate damping	c_m			$[L^1]$		$[L^1]$
Sky-hook air samping	c_{am}			$[L^2]$		$[L^2]$
Piezo-layers resistance	R_e			$[L^{-1}]$		$[L^{-1}]$
Piezo-layers conductance	G_e			$[L^1]$		$[L^1]$
Piezo-layers capacitance	C_e^S			$[L^1]$		$[L^1]$
Cut-off frequency resistive-capacitive	ω_{ce}			$[L^0]$		$[L^0]$
Piezoelectric transduction coefficient	ψ_{pe}			$[L^1]$		$[L^1]$
Electromagnetic power transduction factor	Π_{pe}^2	Eq. (53)		$[L^0]$		$[L^0]$
Harvested power density per 1 g base acceleration Complex optimal load	$\overline{P}_h \Big/ \overline{V}_h\Big\|_{\ddot{w}_h=9.81\ m/s^2}$	Eqs. (81,83)	with air damping Eq. (81) without air damping	$[L^2]$ $[L^2]$		$[L^0]$ $[L^2]$
Harvested power density per 1 g base acceleration Real optimal load	$\overline{P}_{hR} \Big/ \overline{V}_h\Big\|_{\ddot{w}_h=9.81\ m/s^2}$	Eqs. (82,84)	with air damping Eq. (82) without air damping	$[L^3]$ $[L^3]$		$[L^0]$ $[L^2]$
Power harvesting efficiency	E	Eqs. (93,95)	with air damping Eq. (93)	≈ 0.4	≈ 0.4	≈ 0.33
Complex optimal load			without air damping	≈ 0.4	≈ 0.4	≈ 0.4
Power harvesting efficiency	E_R	Eqs. (94,96)	with air damping Eq. (94)	≈ 0	≈ 0.2	≈ 0.25
Real optimal load			without air damping	≈ 0	≈ 0.2	≈ 0.4
Transducer stroke per unit base displacement Complex & real loads	$\frac{w_m - w_h}{w_h}$	Eq. (106)	without air damping with air damping	$[L^1]$ $[L^1]$		$[L^0]$ $[L^1]$

greater than the base displacements. In summary, very large transducer strokes are necessary to obtain the large power harvesting effects at the higher scale range considered in this study. Therefore, as seen for the electromagnetic harvester, large piezoelectric harvesters can function correctly only with small amplitude ambient vibrations.

7. Conclusions

This paper has presented a theoretical study on the scaling laws that characterise the electromechanical response and vibration energy harvesting of meso-scale seismic electromagnetic and piezoelectric transducers assembled from discrete components, which are connected to either complex or purely real optimal harvesting loads and are exposed to harmonic base vibrations at their fundamental natural frequency. The study is based on detailed lumped parameter models, which include the damping effects produced by eddy currents in the electromagnetic transducer and the electrical losses and sky-hook air damping in the piezoelectric transducer, which usually are not taken into consideration. The study has provided equivalent formulations for the responses and for the power harvesting with the two transducers, which, as summarised in Tables 1 and 2, have led to simple formulae that can be used straightforwardly to identify the principal scaling laws that characterise the two harvesters. To this end, the so called electromagnetic and piezoelectric power transduction factors, Π_{cm}^2 and Π_{pe}^2, have been defined in Section 2.3, which characterise the electro-mechanical power transmission of the two transducers with respect to the electrical and mechanical power input into the two transducers.

For conciseness, the principal results of the scaling studies performed on the two harvesters are summarised in Tables 1 and 2. Among the many data produced, it is noteworthy to emphasise that the power transduction factors, which characterise the mechanical to electrical power conversion of the two transducers, are characterised by rather different scaling laws. For instance, the electromagnetic power transduction factor scales proportionally to $[L^2]$ and to $[L^0]$ respectively for small and large scales compared to the $4cm$ reference scale considered in this paper. In contrast, the piezoelectric power transduction factor scales proportionally to $[L^0]$, i.e. it remains constant, in the whole scaling range. These are rather important observations, which indicate that, in general, the electromagnetic transduction is more suited for large scale harvesters, whereas the piezoelectric transduction can be effectively used over a wide scale range.

A second important aspect that has emerged from this study is that, in general, the power harvested with seismic transducers undergoing imposed base vibrations, tends to grow with scale, regardless whether the electromagnetic or the piezoelectric transducer is employed. This is linked to the fact that large scale transducers can actually be characterised by large strokes that thus enables the conversion of larger amount of power per unit base vibration. Of course, this is true for transducer designs capable of withstanding rather large oscillations of bulky suspended masses and for applications where

the source of vibrations has a comparatively much larger mechanical impedance than the base impedance of the transducer. For example large civil constructions (buildings, towers, etc.), transportation infrastructures (e.g. bridges, train tracks, etc.), industrial plants (e.g. heavy machinery, framework structures, cranes, etc.).

A third general conclusion that has emerged from this study is that, eddy currents damping and sky-hook air damping tend to limit the energy harvesting of large electromagnetic and piezoelectric harvesters respectively. Eddy currents damping in electromagnetic harvesters is actually a critical problem even for ordinary scales as the 4*cm* reference scale considered in this paper. Thus, special care must be devoted to the design of the transducer ferromagnetic components to minimise the development of eddy currents. Instead, sky-hook air damping becomes relevant only for very large piezoelectric harvesters.

A final general conclusion regards the efficiency in transforming vibration input power into harvested electrical power. The study has shown that the power harvesting efficiency with the electromagnetic transducer is characterised by an "s-type" scaling law, such that, for small scales, it tends to 0 whereas for large scales it tends to 0.5. This is the result of the intrinsic physics of mechanical to electrical power transfer with electromagnetic transducers, which, as noticed in the analysis of the power transduction factor, tends to 0 for small scales and to a constant value for large scales. When the transducer is affected by eddy currents damping the transition to the limiting value of 0.5 occurs for comparatively larger scales. The power harvesting efficiency with the piezoelectric transducer is instead constant, except for very large scales where it drops because of the sky-hook air damping effect. For perfectly dielectric piezoelectric layers the efficiency is actually equal to 0.5. In practice, in presence of small conductance effects, the efficiency drops to smaller values of the order of 0.3–0.4.

In general, for time-harmonic vibrations at the fundamental natural frequency of the transducers, the energy harvesting with the electromagnetic transducer connected either with the optimal complex or optimal real electric loads produce very similar results. In contrast, a piezoelectric transducer connected to the optimal real electric load harvests comparatively less power than if it were connected to the optimal complex load, particularly for small scales devices. This is due to the fact that, at the fundamental natural frequency, the transducer is characterised by a capacitive electric impedance. Thus, with a real optimal load, the harvester tends to store part of the absorbed energy in the capacitive piezoelectric layers, thus reducing the power harvesting effect. The optimal complex harvesting load compensates exactly this effect, thus allowing the maximum possible power harvesting effect, which is indeed 50% of the power injected in the transducer.

Declaration of competing interests

The authors declare that they have no known competing financial interests or personal relationships that could have appeared to influence the work reported in this paper.

Appendix A. Physical and geometrical properties of the reference harvesters

Tables A1 and A2 below report the physical and geometrical properties of the reference electromagnetic and piezoelectric transducers studied in Ref. [33] and used in this paper as reference transducers with characteristic dimension L = 1.

Table A1
Parameters for the electromagnetic seismic harvester.

Parameters	Value	
Base mass and volume (inner magnet)	$m_b = 115 \times 10^{-3}\ kg$	$V_b = 1.206 \times 10^{-5}\ m^3$
Proof mass and volume (outer ring and coil)	$m_m = 185 \times 10^{-3}\ kg$	$V_m = 3.240 \times 10^{-5} m^3$
Transducer total mass and total volume	$m_{cm} = 300 \times 10^{-3}\ kg$	$V_{cm} = 4.446 \times 10^{-5} m^3$
Transducer footprint area	$A_{cm} = 1.5 \cdot 10^{-3} m^2$	
Magnet radius and length	$R_m = 0.0153m$	$h_m = 0.0165m$
Outer ring volume	$V_y = 2.926 \times 10^{-5} m^3$	
Outer ring electrical conductivity	$\sigma_y = 1.2 \times 10^7 S/m$	
Magnet magnetization per unit length	$M_0 = 10^6 A/m$	
Spiral springs equivalent stiffness	$k_m = 2777\ N/m$	
Fundamental natural frequency	$f_n = 19.5\ Hz$	
Viscous damping coefficient/ratio	$c_a = 0.91\ Ns/m$	$\xi_a = 0.02$
Eddy current damping coefficient/ratio	$c_{ec} = 8.61\ Ns/m$	$\xi_{ec} = 0.19$
Equivalent damping coefficient/ratio	$c_m = 9.52\ Ns/m$	$\xi_m = 0.21$
Electromagnetic transduction factor	$\psi_{cm} = 22.5\ N/A$	
Coil resistance	$R_e = 22\ \Omega$	
Coil lossy inductance constant and exponent	$K_e = 0.034$ $n = 0.78$	
Coil lossy inductance loss factor	$\eta_L = 0.36$	

Table A2
Parameters for the piezoelectric seismic harvester

	Parameters	Value	
Steel substrate	Width and thickness	$b = 20mm$ $h_s = 2\ mm$	
	Length	$L = 140\ mm$	
	Density	$\rho_s = 7800\ kg/m^3$	
	Young's modulus	$Y_s = 20 \times 10^{10} N/m^2$	
	Mass and volume	$m_s = 44 \times 10^{-3}\ kg$	$V_s = 0.56 \times 10^{-5}\ m^3$
Piezoelectric layers	Width and thickness	$b = 20\ mm$ $h_{pe} = 0.15\ mm$	
	length	$L_p = 100\ mm$	
	Density	$\rho_{pe} = 5440\ kg/m^3$	
	Young's modulus	$Y^E_{pe} = 3 \times 10^{10}\ N/m^2$	
	Strain/charge constant	$d_{31} = -170 \times 10^{-12}\ m/V$	
	Permittivity under constant stress	$\varepsilon^T_{33} = 6.3 \times 10^{-9}\ F/m$	
	Electrical conductivity	$\sigma_{pe} = 4.5 \times 10^{-8}\ S/m$	
	Electromechanical coupling factor	$k^2_{31} = 0.14$	
	Mass and volume	$m_{2l} = 3.9 \times 10^{-3}\ kg$	$V_{2l} = 0.06 \cdot 10^{-5}\ m^3$
Lumped elements	Base (block) mass and volume	$m_b = 126 \times 10^{-3}\ kg$	$V_b = 1.76 \times 10^{-5}\ m^3$
	Proof (block) mass and volume	$m_m = 189 \times 10^{-3}\ kg$	$V_m = 2.64 \times 10^{-5}\ m^3$
	Transducer total mass and total volume	$m_{pe} = 363 \times 10^{-3}\ kg$	$V_{pe} = 5.03 \times 10^{-5}\ m^3$
	Transducer footprint area	$A_{pe} = 3.4 \cdot 10^{-3}\ m^2$	
	Equivalent proof mass	$m_m = 215 \times 10^{-3}\ kg$	
	Equivalent stiffness with the piezo-electrodes in short circuit	$k_m = 3369\ N/m$	
	Fundamental natural frequency (short circuit)	$f_n = 20\ Hz$	
	Equivalent viscoelastic damping coefficient and ratio	$c_m = 0.7\ Ns/m$	$\xi_m = 0.013$

Appendix B. Frequency of maximum power transfer

This Appendix presents closed form analytical formulations for the derivation of the frequency at which time-harmonic power harvesting with electromagnetic and piezoelectric seismic harvesters connected to the optimal complex loads is maximised. For both harvesters, the frequency of maximum power harvesting results equal to the fundamental natural frequency of the transducer: i.e. $\omega|_{P_h=max} = \omega_n = \sqrt{k_m/m_m}$. No close form analytical formulation can be derived for the frequency of maximum power harvesting when the two transducers are connected to optimal real loads. However, numerical results have shown that also in this case $\omega|_{P_h=max} = \omega_n = \sqrt{k_m/m_m}$.

B.1. Electromagnetic Harvester

Considering first the electromagnetic harvester, when the optimal complex impedance $Z_{h,opt} = Z^*_{ei}$ is implemented, the frequency dependent harvested power is given by the expression derived in Eq. (59), which can rewritten as follows with respect to the transduction and electrical FRFs T_{ew} and Z_{ei} given in Eqs. (28,29):

$$\overline{P}_h = \frac{1}{8} \frac{\omega^3 m_m \psi_{cm}}{R_e\left(\omega^2 m_m - k_m\right)^2 + \omega^2 c_m\left(\psi^2_{cm} + R_e c_m\right)} |\dot{w}_h|^2. \tag{B.1}$$

As discussed in Section 2.2, at low frequencies below the electrical cut-off frequency $\omega_{ce} = R_e/L_e$, the lossy inductive effect of the coil can be neglected. Thus, setting $\frac{\partial \overline{P}_h}{\partial \omega} = 0$ gives:

$$\frac{m_m \psi_{cm}}{8} \frac{3\omega^2\left[R_e\left(\omega^2 m_m - k_m\right)^2 + \omega^2 c_m\left(\psi^2_{cm} + R_e c_m\right)\right] - \omega^3\left[4R_e\left(\omega^2 m_m - k_m\right)\omega m_m + 2\omega c_m\left(\psi^2_{cm} + R_e c_m\right)\right]}{R_e\left(\omega^2 m_m - k_m\right)^2 + \omega^2 c_m\left(\psi^2_{cm} + R_e c_m\right)} = 0. \tag{B.2}$$

After some mathematical manipulations, this equation can be rewritten in the following form:

$$[R_e c_m]\omega^4 + \left[2\omega_n^2\left(R_e c_m\left(1 - 2\xi^2\right) + 2\xi^2\psi^2_{cm}\right)\right]\omega^2 - 3R_e c_m \omega_n^4 = 0, \tag{B.3}$$

where $\omega_n = \sqrt{k_m/m_m}$ and $\xi = c_m/(2\sqrt{k_m m_m})$ are the mechanical natural frequency and damping ratio of the mechanical part of the transducer. For damping ratios ξ lower than $1/2$, the terms in ξ^2 can be neglected so that Eq. (B.3) can be simplified into the following expression:

$$\omega^4 + \left(2\omega_n^2\right)\omega^2 - 3\omega_n^4 = 0. \tag{B.4}$$

Solving Eq. (B.4) with respect to frequency, the only physically meaningful solution for the frequency of maximum power harvesting results:

$$\omega|_{P_h=max} = \omega_n. \tag{B.5}$$

B.2 Piezoelectric Harvester

Considering now the piezoelectric harvester, when the optimal complex admittance $Y_{h,opt} = Y_{ei}^*$ is implemented, the frequency dependent harvested power is given by the expression derived in Eq. (81), which can rewritten as follows with respect to the transduction and electrical FRFs T_{iw} and Y_{ei} given in Eqs. (37,38):

$$\overline{P}_h = \frac{1}{8}\frac{\omega^3\left(m_m\psi_{pe}\right)^2}{C_e^S\eta_c\left(\omega^2 m_m - k_m\right)^2 + \omega^2 c_m^2 C_e^S\eta_c + \omega c_m\psi_{pe}^2}|\dot{w}_h|^2. \tag{B.6}$$

In this case, setting $\frac{\partial\overline{P}_h}{\partial\omega} = 0$ gives:

$$\frac{4\omega^3\left[G_e\left(\omega^2 m_m - k_m\right)^2 + \omega^2 c_m^2 G_e + \omega^2 c_m\psi_{pe}^2\right] - \omega^4\left[4G_e\left(\omega^2 m_m - k_m\right)\omega m_m + 2\omega c_m^2 G_e + 2\omega c_m\psi_{pe}^2\right]}{\left[G_e\left(\omega^2 m_m - k_m\right)^2 + \omega^2 c_m^2 G_e + \omega^2 c_m\psi_{pe}^2\right]^2} = 0, \tag{B.7}$$

Dividing Eq. (B.7) by $4k_m m_m\omega^2$ and assuming $\omega \neq 0$, after some mathematical manipulations it follows:

$$\left(\frac{\xi\psi_{pe}^2}{\omega_n m_m}\right)\omega^2 - G_e\left(1 - 2\xi^2\right)\omega^2 + G_e\omega_n^2 = 0, \tag{B.8}$$

where, as seen above, $\omega_n = \sqrt{k_m/m_m}$ and $\xi = c_m/(2\sqrt{k_m m_m})$ are the mechanical natural frequency and damping ratio of the mechanical part of the transducer. Also in this case, for damping ratio ξ lower than $1/2$, the terms in ξ^2 can be neglected and thus Eq. (B.8) becomes approximately equal to:

$$\left(\frac{\xi\psi_{pe}^2}{\omega_n m_m}\right)\omega^2 - G_e\omega^2 + G_e\omega_n^2 = 0. \tag{B.9}$$

Since the term $\frac{\xi\psi_{pe}^2}{\omega_n m_m}$ is two orders of magnitude lower with respect to G_e, the above equation can be rewritten as follows:

$$G_e\left(\omega_n^2 - \omega^2\right) = 0. \tag{B.10}$$

Solving Eq. (B.10), the only physically meaningful solution results:

$$\omega|_{P_h=max} = \omega_n. \tag{B.11}$$

References

[1] S. Roundy, P.K. Wright, J. Rabaey, A study of low level vibrations as a power source for wireless sensor nodes, Comput. Commun. 26 (2003) 1131–1144.
[2] H.A. Sodano, D.J. Inman, G. Park, A review of power harvesting from vibration using piezoelectric materials, Shock Vib. Digest 36 (2004) 197–205.
[3] S.P. Beeby, M.J. Tudor, N.M. White, Energy harvesting vibration sources for microsystems applications, Meas. Sci. Technol. 17 (2006) R175–R195.
[4] S.R. Anton, H.A. Sodano, A review of power harvesting using piezoelectric materials (2003–2006), Smart Mater. Struct. 16 (2007) R1–R21.
[5] D.P. Arnold, Review of microscale magnetic power generation, IEEE Trans. Magn. 43 (2007) 3940–3951.
[6] P.D. Mitcheson, E.M. Yeatman, G.K. Rao, A.S. Holmes, T.C. Green, Energy harvesting from human and machine motion for wireless electronic devices, Proc. IEEE 96 (2008) 1457–1486.
[7] K.A. Cook-Chennault, N. Thambi, A.M. Sastry, Powering MEMS portable devices - a review of non-regenerative and regenerative power supply systems with special emphasis on piezoelectric energy harvesting systems, Smart Mater. Struct. 17 (2008).

[8] A. Khaligh, Peng Zeng, Cong Zheng, Kinetic energy harvesting using piezoelectric and electromagnetic technologies—state of the art, IEEE Trans. Ind. Electron. 57 (2010) 850–860.
[9] S. Naifar, S. Bradai, C. Viehweger, O. Kanoun, Survey of electromagnetic and magnetoelectric vibration energy harvesters for low frequency excitation, Measurement 106 (2017) 251–263.
[10] S. Roundy, P.K. Wright, J.M. Rabaey, Energy Scavenging for Wireless Sensor Networks with Special Focus on Vibrations, Springer Science, New York, 2003.
[11] S. Priya, D.J. Inman, Energy Harvesting Technologies, Springer, New York, 2009.
[12] A. Erturk, D.J. Inman, Piezoelectric Energy Harvesting, John Wiley & Sons, Chichester, 2011.
[13] T.J. Kaźmierski, S. Beeby (Eds.), Energy Harvesting Systems, Springer, New York, 2011.
[14] D. Spreemann, Y. Manoli, Electromagnetic Vibration Energy Harvesting Devices: Architectures, Design, Modeling and Optimization, Springer, New York, 2012.
[15] L. Wang, F.G. Yuan, Vibration energy harvesting by magnetostrictive material, Smart Mater. Struct. 17 (2008).
[16] S.D. Moss, O.R. Payne, G.A. Hart, C. Ung, Scaling and power density metrics of electromagnetic vibration energy harvesting devices, Smart Mater. Struct. 24 (2015).
[17] A.D.T. Elliott, L.M. Miller, E. Halvorsen, P.K. Wright, P.D. Mitcheson, Comparison between MEMS and meso scale piezoelectric energy harvesters, Adv. Sci. Technol. 100 (2016) 109–114.
[18] Y.B. Jeon, R. Sood, J. -h. Jeong, S.-G. Kim, MEMS power generator with transverse mode thin film PZT, Sensors Actuators A Phys 122 (2005) 16–22.
[19] W.J. Choi, Y. Jeon, J.-H. Jeong, R. Sood, S.G. Kim, Y. Jeon, V. Corp, K.-D. Korea, Energy harvesting MEMS device based on thin film piezoelectric cantilevers 17, 2006, pp. 543–548.
[20] J. Vanderkooy, A model of loudspeaker driver impedance incorporating eddy currents in the pole structure, J. Audio Eng. Soc. 37 (3) (1989).
[21] W. Marshall Leach, Loudspeaker voice-coil inductance losses: circuit models, parameter estimation, and effect on frequency response, J. Audio Eng. Soc. 50 (6) (2002).
[22] W. Marshall Leach, Introduction to Electroacoustics and Audio Amplifier Design, third ed., Kendall Hunt Publishing Company, Dubuque Iowa, 2008.
[23] S. Sherrit, B.K.B.K. Mukherjee, Characterization of Piezoelectric Materials for Transducers, 2007.
[24] T.L. Jordan, N. Langley, Piezoelectric Ceramics Characterization, ICASE NASA Langley Research Centre, Hampton, Virginia, 2001, p. 23.
[25] C.H. Park, On the circuit model of piezoceramics, J. Intell. Mater. Syst. Struct. 12 (7) (Jul. 2001) 515–522.
[26] M. Karpelson, G.Y. Wei, R.J. Wood, Driving high voltage piezoelectric actuators in microrobotic applications, Sens. Actuators, A Phys. 176 (2012) 78–89.
[27] C.B. Williams, R.B. Yates, Analysis of a micro-electric generator for microsystems, Sensors Actuators A Phys 52 (1996) 8–11.
[28] M. El-hami, P. Glynne-Jones, N.M. White, M. Hill, S. Beeby, E. James, A.D. Brown, J.N. Ross, Design and fabrication of a new vibration-based electromechanical power generator, Sensors Actuators A Phys 92 (2001) 335–342.
[29] P.D. Mitcheson, T.C. Green, E.M. Yeatman, A.S. Holmes, Architectures for vibration-driven micropower generators, J. Microelectromech. Syst. 13 (2004) 429–440.
[30] S.R. Platt, S. Farritor, H. Haider, On low-frequency electric power generation with PZT ceramics, IEEE/ASME Trans. Mechatronics. 10 (2005) 240–252.
[31] N.G. Stephen, On energy harvesting from ambient vibration, J. Sound Vib. 293 (2006) 409–425.
[32] E. Lefeuvre, A. Badel, C. Richard, L. Petit, D. Guyomar, A comparison between several vibration-powered piezoelectric generators for standalone systems, Sensors Actuators A Phys 126 (2006) 405–416.
[33] L. Dal Bo, P. Gardonio, Energy harvesting with electromagnetic and piezoelectric seismic transducers: unified theory and experimental validation, J. Sound Vib. 433 (2018) 385–424.
[34] R.S. Langley, A general mass law for broadband energy harvesting, J. Sound Vib. 333 (2014) 927–936.
[35] M.J. Madou, Fundamentals of Microfabrication: the Science of Miniaturization, CRC Press, 2002.
[36] W.S.N. Trimmer, Microrobots and micromechanical systems, Sensor. Actuator. 19 (1989) 267–287.
[37] P. Gardonio, C. González Díaz, Downscaling of proof mass electrodynamic actuators for decentralized velocity feedback control on a panel, Smart Mater. Struct. 19 (2010).
[38] M. Anthony, B. Scott, P. Shashank, Multiple cell configuration electromagnetic vibration energy harvester, J. Phys. D Appl. Phys. 44 (2011).
[39] P.D. Mitcheson, E.K. Reilly, T. Toh, P.K. Wright, E.M. Yeatman, Performance limits of the three MEMS inertial energy generator transduction types, J. Micromech. Microeng. 17 (2007).
[40] T. O'Donnell, C. Saha, S. Beeby, J. Tudor, Scaling effects for electromagnetic vibrational power generators, Microsyst. Technol. (2007) 26–28.
[41] Z. Yang, S. Zhou, J. Zu, D. Inman, High-performance piezoelectric energy harvesters and their applications, Joule 2 (2018) 642–697.
[42] C. Serre, A. Pérez-Rodríguez, N. Fondevilla, E. Martincic, J.R. Morante, J. Montserrat, J. Esteve, Linear and non-linear behavior of mechanical resonators for optimized inertial electromagnetic microgenerators, Microsyst. Technol. 15 (2009) 1217–1223.
[43] S.P. Beeby, R.N. Torah, M.J. Tudor, P. Glynne-Jones, T. O'Donnell, C.R. Saha, S. Roy, A micro electromagnetic generator for vibration energy harvesting, J. Micromech. Microeng. 17 (2007) 1257–1265.
[44] D.B. Hiemstra, G. Parmar, S. Awtar, Performance tradeoffs posed by moving magnet actuators in flexure-based nanopositioning, IEEE ASME Trans. Mechatron. 19 (1) (2014) 201–212.
[45] C. Paulitsch, P. Gardonio, S.J. Elliott, Active vibration damping using an inertial, electrodynamic actuator, J. Vib. Acoust. 129 (2007) 39–47.
[46] C. González Díaz, C. Paulitsch, P. Gardonio, Active damping control unit using a small scale proof mass electrodynamic actuator, J. Acoust. Soc. Am. 124 (2) (2008) 886–897.
[47] J. Rohlfing, P. Gardonio, S.J. Elliott, Base impedance of velocity feedback control units with proof-mass electrodynamic actuators, J. Sound Vib. 330 (2011) 4661–4675.
[48] E. Turco, P. Gardonio, Sweeping shunted electro-magnetic tuneable vibration absorber: design and implementation, J. Sound Vib. 407 (2017) 82–105.
[49] J. Peirs, Design of Micromechatronic Systems: Scale Laws, Technologies, and Medical Applications, Ph.D. thesis, K.U.Leuven Dept. of Mech. Eng., Leuven, Belgium, 2001.
[50] H.A. Sodano, J.-S. Bae, D.J. Inman, W. Keith Belvin, Concept and model of eddy current damper for vibration suppression of a beam, J. Sound Vib. 288 (2005) 1177–1196.
[51] J.S. Bae, J.H. Hwang, J.S. Park, D.G. Kwag, Modeling and experiments on eddy current damping caused by a permanent magnet in a conductive tube, J. Mech. Sci. Technol. 23 (2009) 3024–3035.
[52] P. Paul, C. Ingale, B. Bhattacharya, Design of a vibration isolation system using eddy current damper, Proc. Inst. Mech. Eng. Part C J. Mech. Eng. Sci. 228 (2014) 664–675.
[53] O. Cugat, J. Delamare, G. Reyne, Magnetic micro-actuators and systems (MAGMAS), IEEE Trans. Magn. 39 (2003) 3607–3612.
[54] D.J. Craik, Magnetism: Principles and Applications, Wiley, Chichester, UK, 1995.
[55] A. Preumont, Mechatronics: Dynamics of Electromechanical and Piezoelectric Systems, Springer, Dordrecht, The Netherlands, 2006.
[56] F.V. Hunt, Electroacoustics: the Analysis of Transduction, and its Background, Acoustical Society of America, New York, 1982.
[57] S. Crandall, D. Karnopp, Dynamics of Mechanical and Electromechanical Systems, McGraw-Hill, New York, 1968.
[58] L. Beranek, T. Mellow, Acoustics: Sound Fields and Transducers, Academic Press, Oxford, 2012.

[59] C.W. Bert, An introductory view of mathematical models, measures, and experimental techniques, J. Sound Vib. 29 (2) (1973) 129–153.
[60] H.T. Banks, D.J. Inman, On damping mechanisms in beams, J. Appl. Mech. 58 (1991) 716.
[61] F. Fahy, P. Gardonio, Sound and Structural Vibration: Radiation, Transmission and Response, Elsevier/Academic, 2007.
[62] K. Uchino, Advanced Piezoelectric Materials: Science and Technology, Woodhead Publishing, Cambridge, UK, 2010.
[63] C. Desoer, The maximum power transfer theorem for n-ports, IEEE Trans. Circ. Theor. 20 (1973) 328–330.
[64] R. Brantley, R. Hanks, D.G. Stephens, The mechanisms and scaling of damping in a practical structural joint, Shock and Vibration Bulletin (1967) 1–8, 36.
[65] S.J. Elliott, M. Zilletti, Scaling of electromagnetic transducers for shunt damping and energy harvesting, J. Sound Vib. 333 (2014) 2185–2195.